広島大学学位請求論文

Doctoral Thesis

Bifurcation of Oscillatory Motion in Self-Propelled Objects at an Air/Water Interface

水面滑走する自己駆動体における振動運動の分岐現象

Mathematical and Life Sciences
Graduate School of Integrated Sciences for Life
Hiroshima University

YU XU

March 2022

Publications

[1] **Yu Xu**, Nami Takayama, Hua Er, Satoshi Nakata*. Oscillatory motion of a camphor object on a surfactant solution. *The Journal of Physical Chemistry B* **2021**, 125, 1674–1679.

[2] **Yu Xu,** Nami Takayama, Yui Komasu, Naho Takahara, Hiroyuki Kitahata, Makoto Iima, Satoshi Nakata*. Self-propelled camphor disk dependent on the depth of the sodium dodecyl sulfate aqueous phase, *Colloids and Surfaces A: Physicochemical and Engineering Aspects*. **2022**, 635, 128087.

[3] **Yu Xu**, Lin Ji, Shunsuke Izumi, Satoshi Nakata*. pH-sensitive oscillatory motion of a urease motor on the urea aqueous solution. *Chemistry an Asian Journal.* **2021**, 16, 1762–1766.

主論文

Bifurcation of Oscillatory Motion in Self-Propelled Objects at an Air/Water Interface

水面滑走する自己駆動体における振動運動の分岐現象

Table of Contents

Chapter 1. General Introduction

1.1 Background

1.1.1 Self-propelled motion and self-propelled object

Self-propelled motion is used to described the autonomous movement of nano-, micro- and macroscale natural and artificial objects [1-5]. In particular, most of the biological systems can regard as self-propelled objects since they can move autonomously by responding to the external environments. For example, schooling swarms of fishes, birds landings, and bacterial chemotaxis, etc [6-9]. In addition, various types of the self-propelled objects in non-living systems have been investigated not only to understand the mechanism of the autonomous motion in the biological systems but also to create the artificial motors that respond to the change in the external environments[10-15], such as, camphor objects [16-18], enzyme motors [19-20], self-propelled droplets [21-22], and Janus particles [23-25]. For the past several years, the mechanisms of the self-propelled motion have been studied, including interfacial phenomena [16-18], bubble [26-27], light [28-29], ultrasound [30], and effect of Marangoni flow [31]. Self-propelled systems have demonstrated potential applications in environmental remediation, biomedicine, separation of organics, etc [33-36]. In addition, the studies of the autonomous motion of the self-propelled object in the non-living system are important to understand the mechanism of chemical energy transformation from a source to movement in biological system [37].

1.1.2 Nonlinear phenomena of the self-propelled systems

In living systems, nonlinear phenomena, including oscillation, synchronization, collective motion, and bifurcation are observed frequently [8, 38-41]. However, self-propelled object in non-living system generally displays unidirectional or random motion. In other words, the autonomy of the non-living system is lower than that of the biological system [16, 17]. For example, a simple camphor boat composed of a camphor disk and a plastic sheet shows a random motion on the surface of the water phase. The mechanism of the self-propelled motion for a camphor boat placed on the water surface have been explained by many reports, as shown in **Figure 1-1**. In a nutshell, a camphor boat floating on the surface of the water phase exhibits continuous motion which driven by the difference in the surface tension around the boat ($\Delta\gamma = \gamma_W - \gamma_c$, γ_W: the surface tension of the pure water (~ 72 mN m^{-1}), γ_c: the surface tension of the saturated camphor aqueous solution (~ 55 mN m^{-1})) [17, 42]. At the initial state, the camphor boat cannot move due to the surface tension of the left edge is the same as that of the right edge. With the diffusion on the right-side water surface of the camphor molecules from the camphor disk, the surface tension of the water phase was reduced by the camphor molecules. Therefore, the camphor object can accelerate by the difference in the surface tension around the camphor boat [17, 42, 43]. In this simple system, the camphor boat exhibits a random motion, this is the autonomy of the camphor object is low.

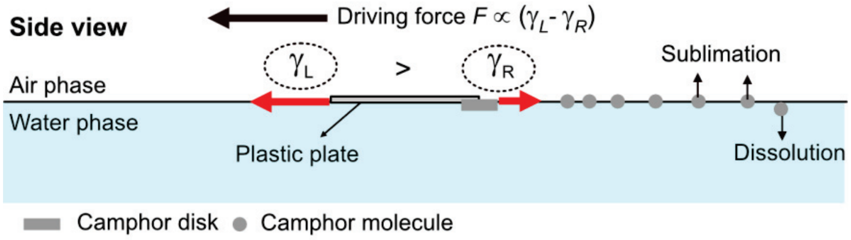

Figure 1-1 Diagram scheme of the mechanism of self-propelled motion for a camphor boat on the water surface.

By introducing nonlinearity into the non-living system can create a self-propelled object with the high autonomy. It is important not only to enhance their diversity of movement and application potential, but also to create a self-propelled motor that exhibits the characteristic motion [16,17]. Various strategies have applied for the non-living system to create nonlinear phenomena [16,17].

Collective motion that defined as the spontaneous behavior of the ordered movement in a system, most of the collective motion is accompanied by synchronization behavior [8]. The synchronization and collective behaviors are often observed in biological systems, for example, in schools of fish, flocks of birds, and herds of animals [8]. The self-propelled particles, like biological systems in nature, also can exhibit the collective motion that responds to change in the external environments [44]. For example, the schooling behavior of micrometer-sized silver chloride particles in water under UV illumination reported by Ibele, et al. [45], and Duan et al. created the exclusion and schooling behaviors of micro-motors using either a chemical or light stimulus [46].

The oscillation phenomenon is defined as the repetition between two or more different states, that have been observed in many fields including physics, chemistry, and biology [40, 41]. For example, Belousov-Zhabotinsky (BZ) reaction [47], and beating heart [48]. In recent years, researchers noticed that the oscillation phenomenon can introduce into self-propelled systems by controlling the shape of the self-propelled object or the external environments [1, 17, 18, 42, 44, 49]. In these systems, the camphor disk as a simple self-propelled object that can induce an oscillatory motion by many approaches. The oscillatory motion is defined that the alteration between resting state and moving state of the self-propelled object [44, 49]. Here, several approaches regarding the generation of the oscillatory motion for the self-propelled object are introduced. Based on the discussion regarding the continuous motion for the camphor boat mentioned above [17], the driving force of the self-motion is the difference in the surface tension induced by the inhomogeneous diffusion of the camphor molecules on the left and right edges [42]. Therefore, the oscillatory motion of the camphor boat on the water surface can be created by controlling the diffusion distance of camphor molecules, which have been reported in our previous study [49]. A camphor boat made by a camphor disk glued on the plastic plate shows the oscillatory motion after placing it on the water surface, see **Figure 1-2**. At the initial resting state, the camphor object has no driving force for acceleration, because the camphor molecules diffuse and accumulate under the plastic plate. The surface tension around the camphor boat is almost near to that of pure water. As the camphor molecules dissolve and diffuse to the edge of the plastic plate, the camphor boat can be driven to move after the amount of camphor molecules reaches a threshold concentration for acceleration. After the camphor moves to a new position, the camphor object returns to the resting state since the disappearance of the driving force. The oscillatory motion was observed because of the repetition between the resting state and the moving state [49].

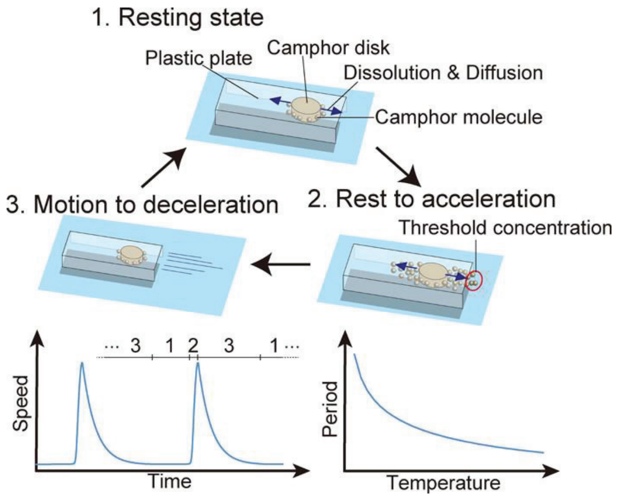

Figure 1-2 The mechanism associated the oscillatory motion for the camphor object. Reprinted with permission from Ref [46], Copyright © 2018 American Chemical Society.

The oscillatory motion of the self-propelled camphor disk on the surfactant aqueous phase is another example. If a camphor disk placed on the surfactant aqueous phase with a low surface tension (< 55 mN m^{-1}), the camphor disk cannot move since the surface tension of saturated camphor aqueous solution is 55 mN m^{-1}. Several types of surfactants have been used to generate characteristic motion of the camphor disk because of the surfactant with the property of reducing the surface tension of water and forming the complex with camphor molecules [49, 50]. For example, the motion modes (e.g., continuous motion, oscillatory motion, and no motion) of the camphor disk were determined by the concentration of the additional surfactant and their alkyl chain length [50]. The complex composed of the camphor and surfactant molecules as a driving force plays an important role in the generation of the oscillatory motion [50-52].

1.1.3 Self-propelled objects coupled with chemical reactions

The products of the chemical reaction can be as the source of the driving force to power the self-propelled objects, such as gas-type products, other products that can reduce the surface tension of the aqueous phase. Several types of self-propulsion objects driven by the products generated by the chemical reaction were explained in this section. The oxygen production decomposed by the hydrogen peroxide ($2\ H_2O_2 \rightarrow 2\ H_2O + O_2$) as the thrust force to drive the self-propelled objects have been reported by many researchers [16, 26, 27]. The mechanism of self-motion associated with these self-propelled objects is the gas bubble propulsion, at first, the gas bubble production generated by the decomposition of the chemical reaction, then released from the surrounding of the self-propelled object, thus driving the self-propelled move to the opposite direction of the gas bubbles [19, 20]. In these self-propelled systems, micro- / nano-motor is a simple and common example, a wide variety of materials (e.g., noble metals including Pt, Au, Fe, enzyme and so on,) have been explored for the preparation and applications of the motors driven by the chemical reaction of hydrogen peroxide. M. Ren et [26], have designed a Junas micromotor made by ethoxylated trimethylolpropane triacrylate/paraffin oil loaded catalysts nanoparticle (Fe_3O_4 and MnO_2), which can promote the degradation of methylene blue dissolved in the water. Fe_3O_4 nanoparticles can not only act as catalysts for pollutant degradation but also control the moving direction. The propulsion bubble for the motor movement form by the product of reaction catalyzed by MnO_2 nano particles in hydrogen peroxide aqueous solution, which further enhanced the degradation of pollutants. For another example, the filter paper immobilizing the catalysts was used to create a self-propelled catalase motor by coupling a chemical reaction, which was reported in previous work of our Lab [53]. In this system, the bifurcation between oscillatory motion and continuous motion of the catalase motor is observed varying the concentration of the hydrogen peroxide aqueous solution. The source of driving force for the self-motion is oxygen bubble produced by the decomposition of the hydrogen peroxide catalyzed by enzyme on the motor. At the rest state, the small oxygen bubbles are produced by the decomposition of the hydrogen peroxide, then several small bubbles form a single large bubble by coalescence, and release from the edge of the catalase motor. Therefore, the catalase motor can be accelerated. After that, the motor will return to the initial resting state because of the bubbles cannot produce continuously for supporting the movement [53]. Therefore, the periodic oscillatory motion of the catalase motor is observed since the repetition between resting state and accelerating state. The average speed of the continuous motion and period of the oscillatory motion are determined by the size of the oxygen bubbles formed under the catalase motor. The nature of the self-motion (e.g., average speed, amplitude, and period) is affected by the generation, growth, and release of the oxygen bubble. In addition to these examples mentioned above, other chemical reactions also can introduce into the self-propelled systems to create a self-propulsion motor, e.g., autonomous motion of BZ droplet coupled with the nonlinear reactions [54, 55], the spontaneous motion of the benzoquinone disk on the reductant aqueous solution (potassium ferrocyanide $K_4Fe(CN)_6$] or ascorbic acid) driven by a redox reaction [15, 56], self-propulsion motion of the camphoric acid motor driven by the acid-base reaction on an alkaline aqueous solution [17, 48, 57], micromotor powered by urea reaction, and so on [20, 23].

1.2 Purpose of this study

The purpose of this doctoral thesis is to create a self-propelled inanimate object by introducing the characteristic nonlinear behavior, which can respond to the internal and external environments. In this research, three self-propelled objects were constructed to study the characteristic motion in non-living systems.

In chapter 2, I would like to construct a self-propelled camphor object consisting of a camphor disk and a plastic sheet to study the influence of the contact area on the self-propulsion. SDS dissolved in a water phase as a surfactant is used to create an oscillatory motion by reducing the surface tension of water. The bifurcation mechanism of motion mode and the feature of the oscillatory motion will discuss based on the number of camphor molecules accumulated at the base of the object and the formation of the SDS–camphor complex.

In chapter 3, I would like to examine the speed of a self-propelled camphor disk placed on SDS aqueous phases at different depths of the aqueous phase. The relationship between speed and water depth at low and high concentrations of SDS will clarify. The mechanism of the experimental phenomenon will discuss in relation to the diffusion rate of camphor molecules developed on the aqueous phase and magnitude of Marangoni flow. In addition, I would like to qualitatively reproduce the experimental phenomenon by numerical calculation based on the Navier-Stokes equation, the reaction-diffusion-advection equation of camphor, and the surface tension of camphor.

Introducing chemical reactions to self-propelled objects is one of the strategies to promote the autonomy and diversity of self-propelled objects in non-living systems. In chapter 4, I would like to design an enzyme motor by coupling an enzyme reaction of the urea. Based on the pH-sensitive activity of urease and the difference in the surface tension around the urease motor, the mechanisms of oscillatory motion and bifurcation of the oscillatory motion and no motion will explain.

1.3 References

[1] W. F. Paxton, K. C. Kistler, C. C. Olmeda, A. Sen, S. K. St. Angelo, Y. Cao, T. E. Mallouk, P. E. Lammert, V. H. Crespi, Catalytic nanomotors: autonomous movement of striped nanorods. *J. Am. Chem. Soc.* **2004**, 126, 13424–13431.

[2] J. Wang, Nanomachines: fundamentals and applications. Wiley VCH, **2013**.

[3] W. Wang, W. Duan, S. Ahmed, T. E. Mallouk, A. Sen, Small Power: Autonomous Nano- and Micromotors propelled by self-generated gradients. *Nano Today* **2013**, 8, 531–534.

[4] R. Dong, Y. Hu, Y. Wu, W. Gao, B. Ren, Q. Wang, Y. Cai, Visible-light driven BiOI-based Janus micromotor in pure water. *J. Am. Chem. Soc.* 2017, 139, 1722–1725.

[5] F. Mou, C. Chen, Q. Zhong, Y. Yin, H. Ma, J. Guan, Autonomous motion and temperature-controlled drug delivery of Mg/Pt-Poly(*N*-isopropylacrylamide) Janus micromotors driven by simulated body fluid and blood plasma. *ACS Appl. Mater. Interface* **2014**, 6, 9897–9903.

[6] H. Berg, D. Brown. Chemotaxis in escherichia coli analysed by three-dimensional tracking. *Nature* **1972**, 239, 500–504.

[7] T. Krell, J. Lacal, F. Muñoz-Martínez, J. A. Reyes-Darias, B. H. Cadirci, C. García-Fontana, J. L. Ramos. Diversity at its best: bacterial taxis. *Environ. Microbiol*. **2011**, 13, 1115–1124.

[8] T. Vicsek, A. Zefeiris, Collective Motion. Physics reports, **2012**, 517, 71–140.

[9] R. Blakemore. Magnetotactic Bacteria. *Science* **1975**, 190, 377–379.

[10] R. Dong, Q. Zhang, W. Gao, A. Pei, B. Ren, Highly efficient light-driven TiO_2–Au Janus micromotors. *ACS Nano* **2016**, 10, 839–844.

[11] H. Wang, M. Pumera, Fabrication of micro/nanoscale motors. *Chem. Rev.* **2015**, 115, 8704–8735.

[12] Y. Li, F. Mou, C. Chen, M. You, Y. Yin, L. Xu, J. Guan, Light-controlled bubble propulsion of amorphous TiO_2/Au Janus micromotors. *RSC Adv*. **2016**, 6, 10697–10703.

[13] J. Li, P. Angsantikul, W. Liu, B. Esteban-Fernandez de Avila, S. Thamphiwatana, M. Xu, E. Sandraz, X. Wang, J. Delezuk, W. Gao, L. Zhang, J. Wang, Micromotors spontaneously neutralize gastric acid for pH-responsive payload release. *Angew. Chem. Int. Ed.* **2017**, 56, 2156–2161.

[14] H. Wang, Z. Sofer, A.Y.S. Eng, M. Pumera, Iridium-catalyst-based autonomous bubble-propelled graphene micromotors with ultralow catalyst loading. *Chem. Eur.*

J. **2014**, 20, 14946–14950.

[15] Y. Matsuda, N. J. Suematsu, S. Nakata, Photosensitive self-motion of a BQ disk. *Phys. Chem. Chem. Phys.* **2012**, 14, 5988–5991.

[16] N. J. Suematsu, S. Nakata, Evolution of self-propelled objects: From the viewpoint of non-linear science. *Chem. Eur. J.* **2018**, 24, 6308–6324.

[17] S. Nakata, V. Pimienta, I. Lagzi, H. Kitahata, N. J. Suematsu, Self-organized motion: physicochemical design based on nonlinear dynamics. *RSC-ebook* **2018**.

[18] S. Nakata, K. Nasu, Y. Irie, S. Hatano, Self-propelled motion of a camphor disk on a photosensitive amphiphilic molecular layer. *Langmuir* **2019**, 35, 4233–4237.

[19] M. Mathesh, J. W. Sun, D. A. Willson, Enzyme catalysis powered micro/nanomotors for biomedical applications. *J. Mater. Chem. B* **2020**, 8, 7319-7334

[20] C. Chen, Z. He, J. Wu, X. Zhang, Q. Xia, H. Ju, Motion of enzyme-powered microshell motors. *Chem. Asian J.* **2019**, 14, 2491–2496.

[21] S. Kaneko, K. Asakura, T. Banno, Phototactic behavior of self-propelled micrometer-sized oil droplets in a surfactant solution. *Chem. Commun.* **2017**, 53, 2237–2240.

[22] Y. Sumino, N. Magome, T. Hamada, K. Yoshikawa, Self-running droplet: Emergence of regular motion from nonequilibrium noise. *Phys. Rev. Lett*. **2005**, 94, 068301

[23] S. Sanchez, L. Soler, J. Katuri, Chemically powered micro- and nanomotors. *Angew Chem. Int. Ed*. **2015**, 54, 1414–1444.

[24] P. Schattling, B. Thingholm, B. Stadler, Enhanced diffusion of glucose-fueled Janus particles. *Chem. Mater*. **2015**, 27, 7412–7418.

[25] L. Zhao, Y. Liu, S. Xie, P. Ran, J. Wei, Q. Liu, X. Li, Janus micromotors for motion capture-ratiometric fluorescence detection of circulating tumor cells. *Chem. Eng. J.* **2020**, 382, 123041–1230412.

[26] K. Villa, C. L. Manzanares Palenzuela, Z. Sofer, S. Matejkova, M. Pumera, Metal free visible-light photoactivated C_3N_4 bubble-propelled tubular micromotors with inherent fluorescence and on/off capabilities. *ACS Nano* 2018, 12, 12482–12491.

[27] M. Ren, W. Guo, H. Guo, X. Ren, Microfluidic fabrication of bubble-propelled micromotors for wastewater treatment. *ACS Appl. Mater. Inter.* 2019, 11, 22761–22767.

[28] C. Chen, F. Mou, L. Xu, S. Wang, J. Guan, Z. Feng, Q. Wang, L. Kong, W. Li, J. Wang, Q. Zhang, Light-steered isotropic semiconductor micromotors. *Adv. Mater.* **2017**, 29, 1603374.

[29] M. Xiao, C. Jiang, F. Shi, Design of a UV-responsive micro actuator on a smart device for light-induced on-off-on motion. *NPG Asia Mater.* **2014**, *6*, e128.

[30] W. Wang, L. A. Castro, M. Hoyos, T. E. Mallouk, Autonomous motion of metallic microrods propelled by ultrasound. *ACS Nano* **2012**, 6, 6122–6132.

[31] H. Kitahata, S. Hiromatsu, Y. Doi, S. Nakata, M. R. Islam, Self-motion of a camphor disk coupled with convection. *Phys. Chem. Chem. Phys.* **2004**, 6, 2409−2414.

[32] T. Maric, M. Z. M. Nasir, N. F. Rosli, M. Budanovic, R. D. Webster, N. J. Cho, M. Pumera, Microrobots derived from variety plant pollen grains for efficient environmental clean up and as an anti-cancer drug carrier. *Adv. Funct. Mater*. **2020**, 30 2000112.

[33] J. Wang, R. Dong, Q. Yang, H. Wu, Z. Bi, Q. Liang, Q. Wang, C. Wang, Y. Mei, Y. Cai, One body, two hands: photocatalytic function- and fenton effect integrated light-driven micromotors for pollutant degradation. *Nanoscale* **2019**, 11, 16592–16598.

[34] P. Dhar, S. Narendren, S. S. Gaur, S. Sharma, A. Kumar, V. Katiyar, Self-propelled cellulose nanocrystal based catalytic nanomotors for targeted hyperthermia and pollutant remediation applications. *Int. J. Biol. Macromol.* **2020**, 158, 1020–1036.

[35] D. Rojas, B. Jurado-Sanchez, A. Escarpa, Shoot and sense Janus micromotorsbased strategy for the simultaneous degradation and detection of persistent organic pollutants in food and biological samples. *Anal. Chem*. **2016**, 88, 4153–4160.

[36] Z. Lin, Z. Wu, X. Lin, Q. He, Catalytic polymer multilayer shell motors for separation of organics. *Chem. Eur. J.* **2016**, 22, 1587–1591.

[37] W. Bechtel, A. Bollhagen, Active biological mechanisms: transforming energy into motion in molecular motors. *Synthese* **2021**, 198, 1–25.

[38] M. Theves, J. Taktikos, V. Zaburdaev, H. Stark, C. Beta. A bacterial swimmer with two alternating speeds of propagation. *Biophys J.* **2013**, 105, 1915–1924.

[39] Y. Bao, E. Pöppel, L. Wang, X. Lin, T. Yang, M. Avram, J. Blautzik, M. Paolini, S. Silveira, A. Vedder, Y. Zaytseva,B. Zhou, Synchronization as a biological, psychological and social mechanism to create common time: A theoretical frame and a single case study. *Psych J.* **2015**, 4, 243-254.

[39] Y. X. Li, R. Lukeman, L. Edelstein-Keshet. Minimal mechanisms for school formation in self-propelled particles. *Physica D: Nonlinear Phenomena* **2007**, 237, 699–720.

[40] W. O. Friesen, G. D. Block, What is a biological oscillator. *Am J Physiol.* **1984**, 246, 847–853.

[41] D. B. Forger, Biological clocks, rhythms, and oscillations: the theory of biological timekeeping. Cambridge. MIT Press, **2017**.

[42] Tomlinson, C. On the motion of camphor on the surface of water. *Proc. R. Soc.* London **1862**, 11, 575–577.

[43] R. Golestanian. Collective behavior of thermally active colloids. *Phys Rev Lett.* **2012**, 108, 038303.

[44] S. Nakata, H. Yamamoto, Y. Koyano, O. Yamanaka, Y. Sumino, N. J. Suematsu, H. Kitahata, P. Skrobanska, J. Gorecki, Selection of the rotation direction for a camphor disk resulting from chiral asymmetry of a water chamber. *J. Phys. Chem. B* **2016**, 120, 9166−9172.

[45] M. Ibele, T. Mallouk, A. Sen, Schooling behavior of light-powered autonomous micromotors in water. *Angew Chem. Int. Ed.* **2009**, 48, 3308-3312.

[46] W. T. Duan, R. Liu, A. Sen, Transition between collective behaviors of micromotors in response to different stimuli. *J. Am. Chem. Soc.* **2013**, *135*, 1280–1283.

[47] B. P. Belousov, A periodic reaction and its mechanism. In: Oscillations and traveling waves in chemical systems. Wiley, New York, **1985**.

[48] A. Babloyantz, A. Destexhe, Is the normal heart a periodic oscillator. *Biol. Cybern.* **1988**, 58, 203–211.

[49] R. Tenno, Y. Gunjima, M. Yoshii, H. Kitahata, J. Gorecki, N. J. Suematsu, S. Nakata, Period of oscillatory motion of a camphor boat determined by the dissolution and diffusion of camphor molecules. *J. Phys. Chem. B* **2018**, 122, 2610−2615.

[50] S. Nakata, M. Murakami, Self-motion of a camphor disk on an aqueous phase depending on the alkyl chain length of sulfate surfactants. *Langmuir* **2010**, 26, 2414−2417.

[51] S. Nakata, J. Kirisaka, Y. Arima, T. Ishii, Self-motion of a camphanic acid disk on water with different types of surfactants. *J. Phys. Chem. B* **2006**, 110, 21131−21134.

[52] S. Nakata, R. Tenno, A. Deguchi, H. Yamamoto, Y. Hiraga and S. Izumi, Marangoni flow around a camphor disk regenerated by the interaction between camphor and sodium dodecyl sulfate molecules. *Colloids Surf. A* **2015**, 466, 40–44.

[53] S. Nakata, M. Nomura, H. Yamamoto, S. Izumi, N. J. Suematsu, Y. Ikura, T. Amemiya, Periodic Oscillatory Motion of a Self-Propelled motor driven by decomposition of H_2O_2 by catalase. *Angew. Chem. Int. Ed.* **2017**, 56, 861−864.

[54] N. J. Suematsu, Y. Mori, T. Amemiya, S. Nakata, Oscillation of speed of a self-propelled Belousov-Zhabotinsky droplet. *J. Phys. Chem. Lett.* **2016**, 7 , 3424–3428.

[55] N. J. Suematsu, Y. Mori, T. Amemiya, S. Nakata, Spontaneous mode switching of self-propelled droplet motion induced by a clock reaction in the Belousov-Zhabotinsky medium. *J. Phys. Chem. Lett.* **2021**, 12, 7526–7530.

[56] N. J. Suematsu, Y. Miyahara, Y. Matsuda, S. Nakata, Self-motion of a benzoquinone disk coupled with a redox reaction. *J. Phys. Chem. C* **2010**, 114, 13340–13343.

[57] S. Nakata, J. Kirisaka, Characteristic motion of a camphanic acid disk on water depending on the concentration of triton X-100. *J. Phys. Chem. B* **2006**, 110, 1856–1859.

Chapter 2. Oscillatory motion of a self-propelled camphor object on the surface of surfactant aqueous phase

2.1 Introduction

Various kinds of the self-propelled objects have been investigated not only to understand the mechanism of the autonomous motion in the living systems but also to create the artificial motors that respond to the change in the external environments [1, 2], such as chemotaxis [3-7], and collective motion [8-10]. However, most self-propelled objects in non-living systems display unidirectional or random motion [2, 11]. In other word, the autonomy of self-propelled motors in living system is generally higher than that in living system, because nonlinear phenomena are often observed in living system [12-14]. In order to promote the autonomy and diversity of self-propelled object in non-living system, various strategies have applied for the non-living system to create nonlinear behavior [15-22].

A camphor disk or boat upon the water surface can be regarded as a simple self-propelled object because the shape and size of camphor particle are easy to manufacture and the enables sustained autonomous motion, ca. 1 h [2, 23]. The driving force of self-propelled motion for the camphor object is the difference in the surface tension induced by the concentration gradient of camphor around the object [24, 25]. Various characteristic motion modes of the self-propelled camphor objects that are sensitive to the internal or external environments have been reported in our previous researches, for instance, the chamber shapes or the camphor objects [26, 27], depth of the water phase [28, 29], and additional surfactants [31]. In addition, several applied systems have also been studied, for example, collective motion [32], and energy transduction [33]. In one of the studies mentioned above, the characteristic self-propelled motion for the camphor disk floating on the surface of the sodium dodecyl sulfate (SDS) aqueous phase was investigated to control the mode-switching of the self-motion by additional chemicals [31]. In such a camphor–SDS system, the features of the self-propelled motion were determined by the concentration of SDS, as the concentration of SDS increases, the four motion mode, including the continuous motion with higher speed, oscillatory motion, continuous motion with lower speed, oscillatory motion, and no motion were observed [31]. The oscillatory motion is generated above the critical micelle concentration (CMC ~ 8.0 mM) of SDS since the interaction between the camphor and SDS molecules increases the dissolution rate of camphor in the water phase. In addition, the complexes composed of the SDS and camphor molecules play an important role in the generation of oscillatory motion [2, 31].

However, the features of motion and mechanism of self-motion for the camphor disk floating on the surfactant aqueous phase based on the kinetics of camphor and surfactant molecules has not been clarified thus far. In this chapter, I examined the features of oscillatory motion by controlling the amount of camphor molecules dissolved from the disk into the SDS aqueous phase. These experimental results indicate that the nature of the oscillatory motion is determined by the amount of camphor molecules accumulated at the base of the self-propelled object [35].

2.2 Experimental section

2.2.1 Chemicals and materials

Sodium dodecyl sulfate, SDS ($C_{12}H_{25}OSO_3Na$, purity > 98%, CAS 151-21-3), (+)–Camphor ($C_{10}H_{16}O$, > 98%, CAS 76-22-2), and 7-hydroxycoumarin ($C_9H_6O_3$, purity > 99%, CAS 93-35-6) were purchased from Sigma-Aldrich (St. Louis, MO), Wako Chemicals (Kyoto, Japan), and INDOFINE Chemical Company, Inc. (Stryker Lane, Hillsborough), respectively. Water was distilled by the Auto Still model system (Yamato Scientific Co., Ltd., WG 23, Tokyo, Japan) *via* an ion exchange resin filter. Two camphor objects (Objects I and II) using in this study, as shown in **Figure 2-1**. Object I was made by a camphor disk (diameter: 7.0 mm; thickness: 1.0 mm; mass: 38

mg) and a circular plastic sheet (thickness: 0.1 mm). Object II was made by a same camphor disk and a plastic ring (outer diameter: 7.0 mm; thickness: 0.1 mm). The camphor disk was manufactured using a Fourier transform infrared spectroscopy (FT-IR) pellet die, and the plastic sheet and ring made of polyethylene terephthalate were covered on the bottom center in the camphor disk using by glue. The contact area between the bottom of the disk and the SDS aqueous phase (S in mm^2) as a variable parameter was changed using a circular plastic sheet with different diameters (d_p in mm) for Object I or a plastic ring with different inner diameters (d_i in mm) for Object II. The relationship between S and diameters for Objects I and II is shown in **Figure 2-2**.

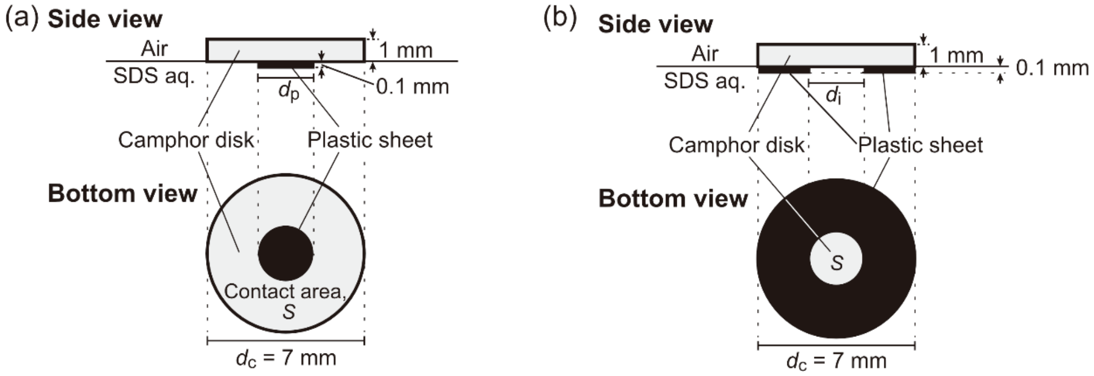

Figure 2-1. Schematic diagram of the camphor objects ((a) Object I and (b) Object II) used in this study. d_c denotes the diameter of the camphor disk. d_p denotes the diameter of the circular plastic sheet in Object I. d_i denotes the inner diameter of the plastic ring in Object II. S denotes the contact area between the bottom of the disk and the SDS aqueous phase. The concentration of SDS aqueous solution was 10 mM.
Reprinted with permission from *J. Phys. Chem. B* **2021**, 125, 1674–1679. Copyright © 2021, American Chemical Society.

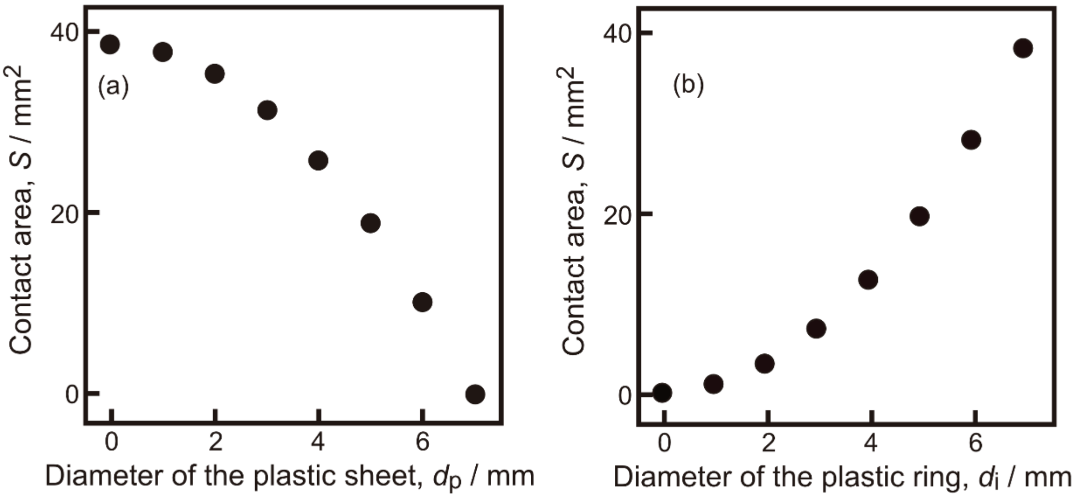

Figure 2-2. Contact area (*S*) of a camphor object as a function of the diameter of object (a) the diameter of the plastic sheet in Object I (d_p), and (b) the inner diameter of the plastic ring in Object II (d_i).

Reprinted with permission from *J. Phys. Chem. B* **2021**, 125, 1674–1679. Copyright © 2021, American Chemical Society.

2.2.2 Observation of the movements for the camphor object

The camphor objects I and II were placed on the surface of the SDS aqueous phase (concentration: 10 mM; water level: 3.0 mm; volume: 30 mL) in a glass Petri dish (diameter: 120 mm). The motion of the camphor objects was recorded adopting a digital video camera (SONY, HDR-CX430, minimum time resolution: 1/30 s, Tokyo, Japan) at room temperature ($T = 298 \pm 2$ K) from a top view. The movies were analyzed using a Java image processing and analysis program "ImageJ 1.41" (National Institutes of Health, Bethesda, MD, USA). SDS aqueous solutions and camphor objects were exchanged for the individual examinations, and at least three examinations were performed for the individual experimental conditions.

2.2.3 Visualization of the diffusion of the camphor molecules

To visualize the diffusion of camphor molecules from the camphor disk on the surface of SDS aqueous solution, a kind of indicator named by 7-hydroxycoumarin was homogeneously blended with camphor by 1 w/w% to produce a camphor disk, since it can be clearly observed by a camera under a UV light irradiation condition. In the other hand, based our experimental results, I considered that 7-hydroxycoumarin have no effect on the movements of the camphor object since a 7-hydroxycoumarin disk floating on water exhibited no motion. Additionally, our experimental result shows that the surface tension of 1 mM of 7-hydroxycoumarin aqueous solution is 71.9 ± 0.2 mN m^{-1}. Meanwhile, the physicochemical properties (solubility in water, density, and molecular weight) of the camphor were more similar to those of 7-hydroxycoumarin, compared to the other indicators including the fluorescein potassium salt. The camphor disk (diameter: 7.0 mm; thickness: 1.0 mm; mass: 38 mg) after the additional of a small amount of 7-hydroxycoumarin was fixed on the surface of SDS aqueous solution (concentration: 10 mM; volume: 30 mL; water level: 3.0 mm) in a glass Petri dish (diameter: 120 mm), and then diffusion behavior was recorded adopting a camera under a UV light irradiation of 365 nm in wavelength (AS ONE Corporation, Handy UV Lamp UV-16, Osaka, Japan) from the top in a dark box. The concentration of 7-hydroxycoumarin (C_{hc}) around camphor disk was evaluated by the difference in gray value (ΔGV), ΔGV was calculated by the intensity of the emitted blue color using ImageJ software.

2.2.4 Evaluation of the concentration of camphor

To evaluate the concentration of camphor molecules dissolved into the SDS aqueous solution, a free camphor object (Object I) was placed on the surface of the SDS aqueous phase (volume: 2 mL; water level: 2.0 mm) in a glass Petri dish (diameter: 37 mm). After 40 s, a small volume (0.5 mL) of SDS solution mixed with the dissolved camphor molecules was extracted from the solution near the aqueous surface around the camphor object by a syringe. Then, the absorbance of the mixed aqueous solution including SDS and camphor was measured adopting a UV-Visible spectrophotometer (UV-1650, Shimadzu Corporation, Kyoto, Japan) by a small Y-shaped quartz cell (length: 1 mm; width: 1 mm; high: 4.5 mm; volume: 0.5 mL).

2.3 Results

Figure 2-3 shows the time series of the speed for a camphor object I placed on the surface of a 10 mM SDS aqueous phase at different *S* (*S* = (a) 10.2, (b)18.9, (c) 25.9, (d) 31.4, (e) 35.3, and (f) 38.5 mm^2). Two types of motion mode, oscillatory (alternation between resting state and moving state) and no motion, were observed at different *S*, this is, no motion of the camphor object observed at $S = 10.2$ mm^2 in **Figure 2-3 (a)**, oscillatory motion was observed at $S \geq 18.9$ mm^2 in **Figure 2-3 (b)-(f)**. The oscillatory motion of the camphor object under the each condition was maintained for at least 30 min. The period of oscillatory motion at $S = 18.9$ mm^2 was clearly longer than that at $S = 25.9$ mm^2, but with an increase in *S* at $S \geq 25.9$ mm^2, significant change in the period of oscillation was not observed. In contrast, the amplitude of oscillatory motion increased with an increase in *S*. Here, I define the period of oscillatory motion to be a time interval of repetition between neighbor maximum speed.

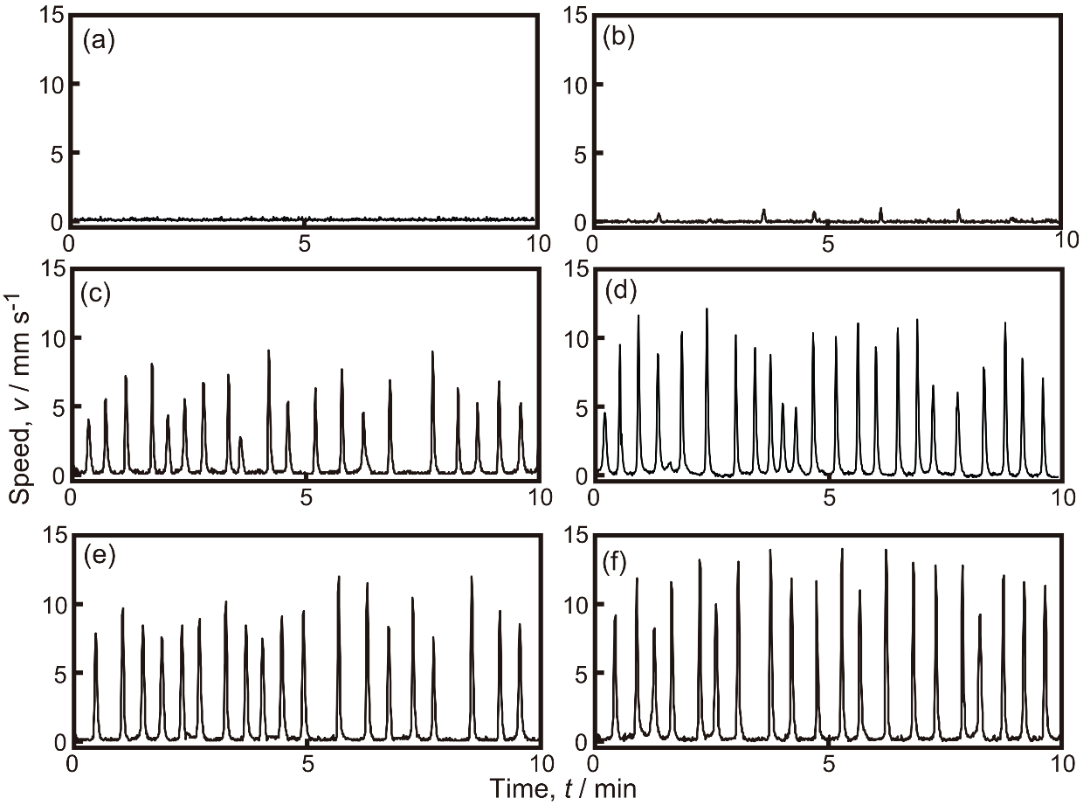

Figure 2-3. Time series of the speed for a camphor object (Object I) at S = (a) 10.2, (b)18.9, (c) 25.9, (d) 31.4, (e) 35.3, and (f) 38.5 mm^2. $t = 0$ when the object was floated on the surface of 10 mM SDS aqueous solution.
Reprinted with permission from *J. Phys. Chem. B* **2021**, 125, 1674–1679. Copyright © 2021, American Chemical Society.

The motion of the self-propelled camphor object II in **Figure 2-1** was examined in order to clarify the effect of the shape of the plastic plate on the feature motion of the camphor object. **Figure 2-4** shows the time variation of the speed for a camphor object II on a 10 mM SDS aqueous surface at different S values (S = (a) 12.6, (b)19.6, (c) 28.3, (d) 38.5 mm^2.). No motion was observed at S = 12.6 mm^2. Oscillatory motion was observed at S > 19.6 mm^2. The period of oscillatory motion was decreased with an increase in S. In contrast, the amplitude of oscillatory motion increased with an increase in S.

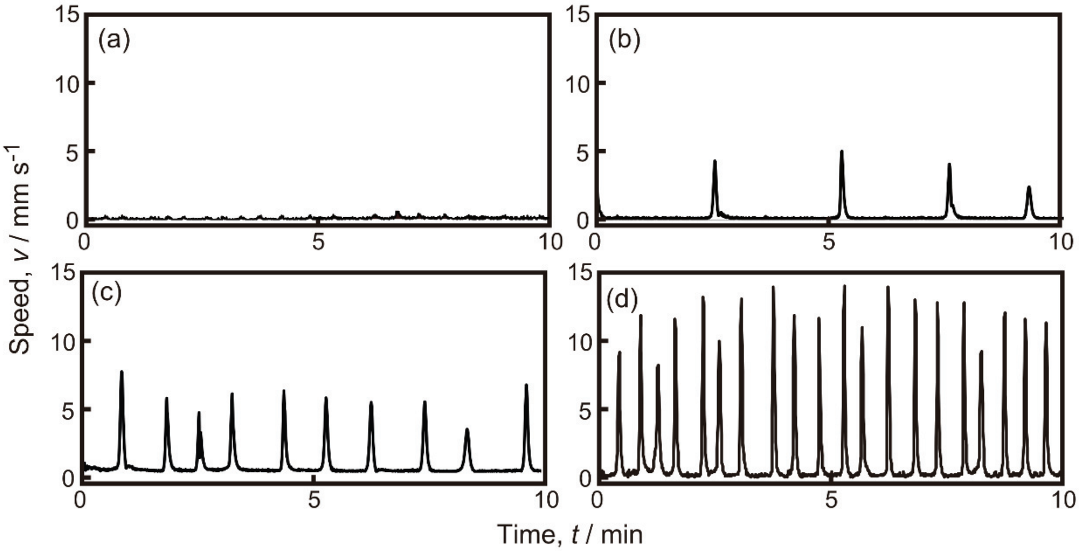

Figure 2-4. Time series of the speed of a camphor object (Object II) at S = (a) 12.6, (b)19.6, (c) 28.3, (d) 38.5 mm^2. $t = 0$ when the object was placed on the surface of 10 mM SDS aqueous phase.

Reprinted with permission from *J. Phys. Chem. B* **2021**, 125, 1674–1679. Copyright © 2021, American Chemical Society.

Figure 2-5 shows (a) the frequency, f, and (b) maximum speed of the oscillatory motion, v_{max}, for the camphor object (Object I) as a function of S. Here, $v = 0.5$ mm·s^{-1} was defined as a threshold value of the speed between motion and no motion. Oscillatory motion and no motion were observed $S \geq 18.9$ mm^2 and at $S < 18.9$ mm^2, respectively. This is, bifurcation between oscillatory motion and no motion was occurred around $S = 18.9$ mm^2. With an increase in S, the frequency of oscillatory motion was increased at $10.2 \leq S \leq 25.9$ mm^2, but was almost constant at ~ 0.03 s^{-1} at $S \geq 25.9$ mm^2. However, as S increases, maximum speed of oscillatory motion was increased linearly at $S \geq 18.9$ mm^2.

Figure 2-6 shows (a) frequency and (b) the maximum speed of oscillatory motion for the camphor object II as a function of S. Oscillatory motion and no motion were observed at $S \geq 19.6$ mm^2 and $S < 19.6$ mm^2, respectively. In other words, bifurcation of the motion mode between no motion and oscillatory motion was observed around $S = 19.6$ mm^2. With an increase in S, the frequency and v_{max} of oscillatory motion were increased with an increase in S at $S \geq 19.6$ mm^2.

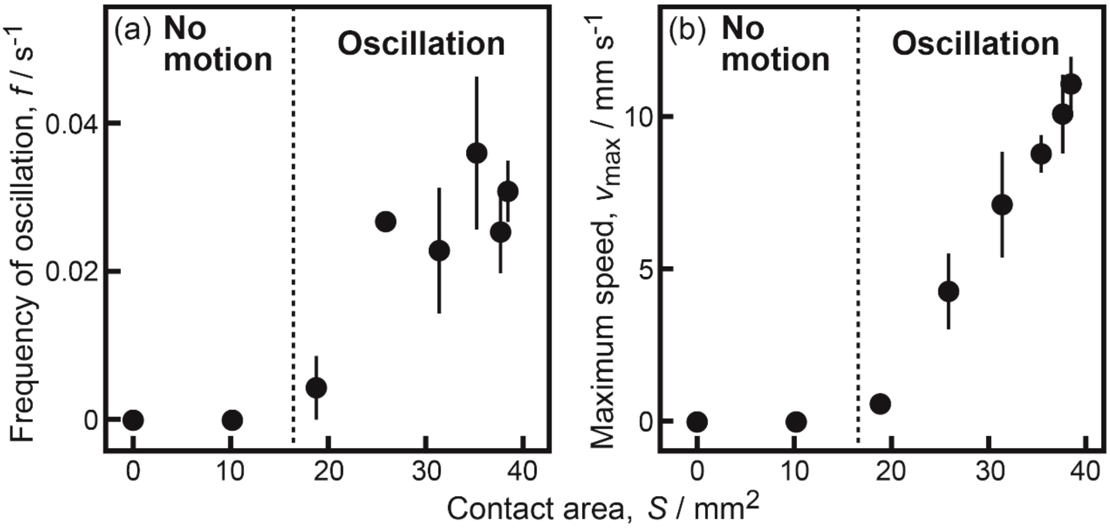

Figure 2-5. (a) Frequency and (b) $v_{\max}$ of the camphor object (Object I) as a function of S. The error bars corresponds to the standard deviation were obtained from three examinations including at least 10 oscillations.
Reprinted with permission from *J. Phys. Chem. B* **2021**, 125, 1674–1679. Copyright © 2021, American Chemical Society.

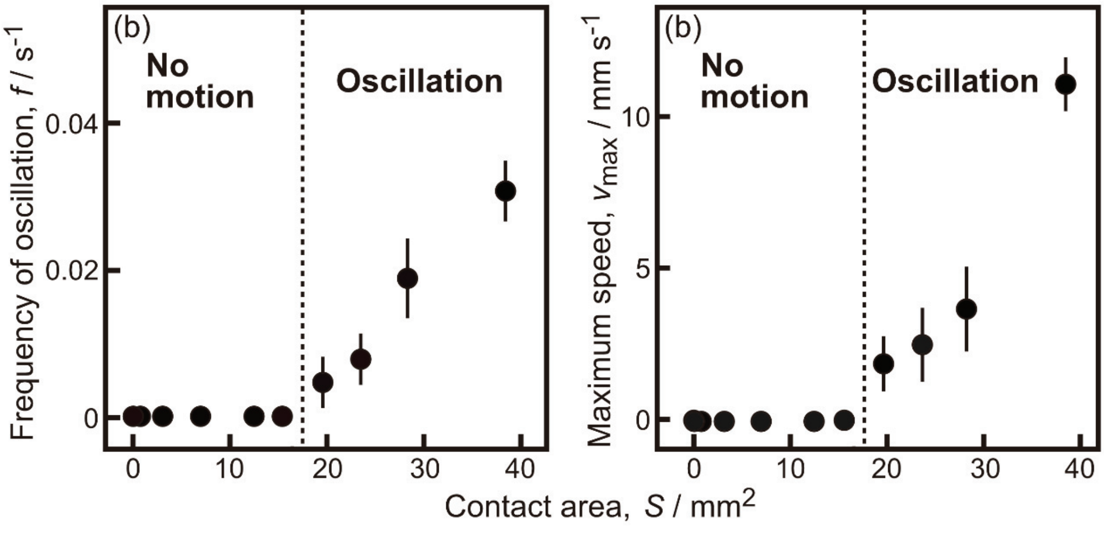

Figure 2-6. (a) Frequency and (b) $v_{\max}$ of oscillatory motion of the camphor object (Object II) depending on the contact area (S / mm^2). The error bars corresponds to the standard deviation were obtained from three examinations including at least 10

oscillations.
Reprinted with permission from *J. Phys. Chem. B* **2021**, 125, 1674–1679. Copyright © 2021, American Chemical Society.

The time profiles of the speed and v_{max} at different values of S for a single oscillation of camphor object I were compared to clarify the acceleration process in the oscillatory motion, as indicated in **Figure 2-7**. Here, the time required to reach from zero to the maximum speed is called the acceleration time (t_m) in this study. The similar acceleration profiles were observed at different S, as indicated in **Figure 2-7a**. The relationship between v_{max} and t_m was also similar to the graph on the time variation of the speed during the acceleration for S = 38.5 mm^2, as indicated in **Figure 2-7b**.

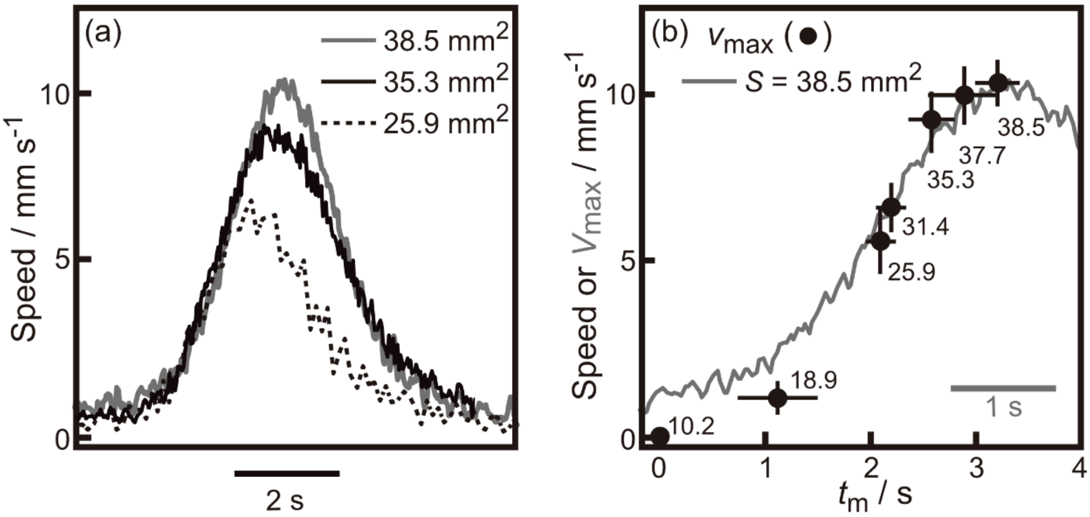

Figure 2-7. (a) Time series of the speed for an individual oscillation of the camphor objects (Object I) with different S (dotted line: 25.9 mm^2, black line: 35.3 mm^2, gray line: 38.5 mm^2) and (b) relationship between v_{max} and t_m at different S (filled circles) together with the time variation of the speed for a single oscillation at S = 38.5 mm^2 (gray line). t_m was defined as zero when the camphor object changed from resting state to motion, i.e., the speed was over 0.5 mm s^{-1} from zero. The numbers in (b) denote the values of S (mm^2). The error bars corresponds to the standard deviation were obtained from at least three examinations.
Reprinted with permission from *J. Phys. Chem. B* **2021**, 125, 1674–1679. Copyright © 2021, American Chemical Society.

Here, I performed the Evaluation I to clarify the effect of S on the amount of camphor dissolved from the camphor object I. In this section, the difference in the gray value (ΔGV) was measured at different concentrations of 7-hydroxycoumarin aqueous solution (C_{hc}) to obtain a calibration curve. ΔGV was defined as 0 for 10 mM SDS aqueous solution without 7-hydroxycoumarin. The calibration curve on ΔGV *versus* C_{hc} of 7-hydroxycoumarin aqueous solution is shown in **Figure 2-8**. ΔGV was approximately proportional to C_{hc}, as indicated in **eq 2-1**.

$$C_{\mathrm{hc}} = 1.02\ \Delta GV. \qquad (2\text{-}1)$$

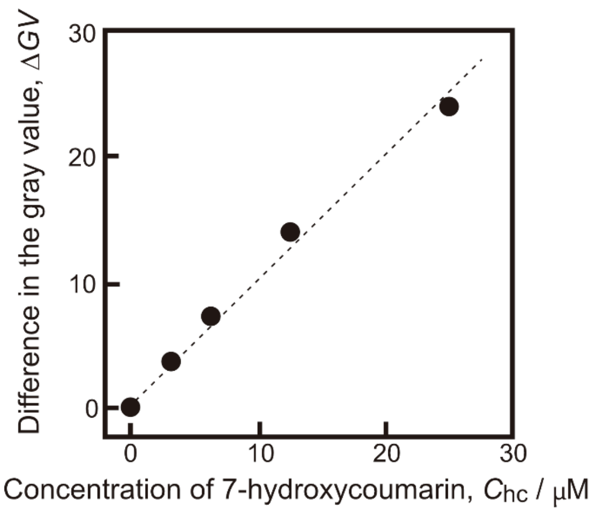

Figure 2-8. Relationship between the difference in the gray value (ΔGV) and the concentration of 7-hydroxycoumarin solution (C_{hc}).

Reprinted with permission from *J. Phys. Chem. B* **2021**, 125, 1674–1679. Copyright © 2021, American Chemical Society.

7-Hydroxycoumarin was used as an indicator under the UV light irradiation to visualize the distribution of camphor molecules around the camphor object placed on 10 mM SDS aqueous phase. The average value of difference in the gray value (ΔGV) of 1 w/w% 7-hydroxycoumarin was obtained by **eq 2-2**.

$$\Delta GV = \frac{(GV_a - GV_{\mathrm{a}'}) + (GV_b - GV_{\mathrm{b}'}) + (GV_c - GV_{\mathrm{c}'}) + (GV_d - GV_{\mathrm{d}'})}{4}, \qquad (2\text{-}2)$$

where GV_p (p = a, b, c, d, a', b', c', and d') are the gray values of 1 w/w% 7-hydroxycoumarin at the points $P_a(0, y_1)$, $P_b(x_1, 0)$, $P_c(0, -y_1)$, $P_d(-x_1, 0)$, $P_{a'}(0, y_2)$ $P_{b'}(x_2, 0)$, $P_{c'}(0, -y_2)$, and $P_{d'}(x_2, 0)$, respectively. The coordinate of the center of the camphor object as (0, 0), $x_1 = y_1 = 6.5$ mm, $x_2 = y_2 = 20.0$ mm (see **Figure 2-9**). $GV_a - GV_{a'}$ is the difference value of GV between two points, P_a where 7-hydroxycoumarin molecules exist and $P_{a'}$ where 7-hydroxycoumarin molecules don't exist on the water phase. Here, t_o was defined as the observation time, and $t_o = 0$ when the camphor object was touched to the aqueous surface. **Figure 2-10** shows the snapshots of the distribution of 7-hydroxycoumarin around the camphor object (Object I). The distribution area was increased with an increase in time. Here, I selected $t_o = 40$ s which was close to one period of the oscillatory motion. **Figure 2-11** shows ΔGV of 7-hydroxycoumarin around the camphor object (Object I) at $t_o = 40$ s depending on S.

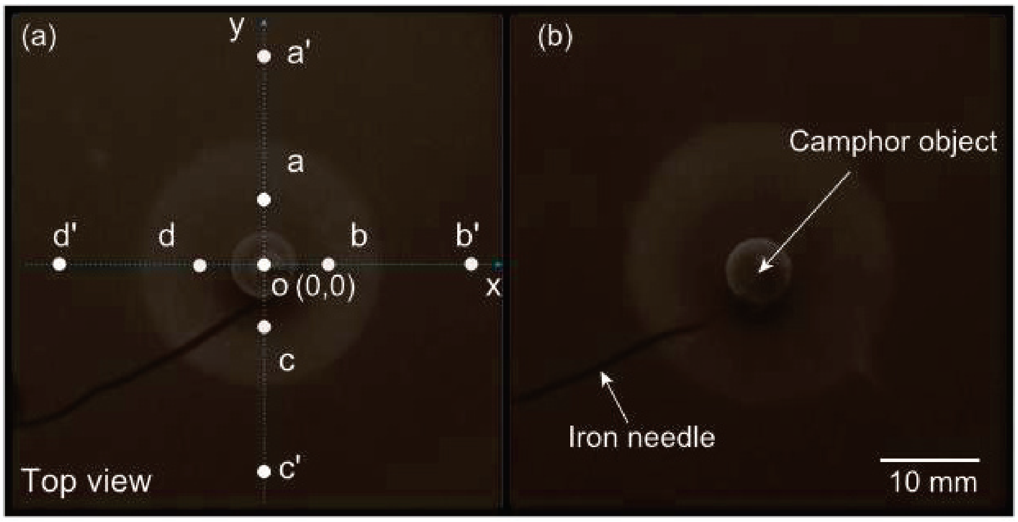

Figure 2-9. Locations of the points to measure the gray value, $P_a(0, y_1)$, $P_b(x_1, 0)$, $P_c(0, -y_1)$, $P_d(-x_1, 0)$, $P_{a'}(0, y_2)$ $P_{b'}(x_2, 0)$, $P_{c'}(0, -y_2)$, and $P_{d'}(-x_2, 0)$, $x_1 = y_1 = 6.5$ mm, $x_2 = y_2 = 20.0$ mm. The points are 6.5 and 20.0 mm apart from the center of the camphor object, which is located at o(0, 0), on x and y axes. The range of the dissolution length, L_1, was 6.5 mm < L_1< 20.0 mm, L_1 refers to the distance between the edge of the distribution profile and the center of the camphor object (Object I), this means that GV of P_a and $P_{a'}$ can represent the gray value of the point where 7-hydroxycoumarin molecules exist and don't exist on the water phase, respectively. $t_o = 40$ s, S = (a) 35.3 and (b) 10.2 mm^2. The camphor object was fixed on water using an iron needle (diameter: 1 mm, length: 150 mm).

Reprinted with permission from *J. Phys. Chem. B* **2021**, 125, 1674–1679. Copyright © 2021, American Chemical Society.

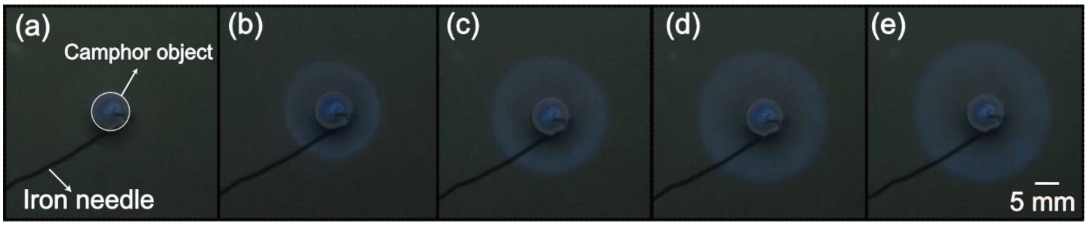

Figure 2-10. Snapshots of the distribution of 7-hyrdoxycoumarin molecules for S = 35.3 mm^2 of Object I (top view). t_o = (a) 0, (b) 10, (c) 20, (d) 30, and (e) 40 s. The blue emission color, which exhibits the existence of 7-hyrdoxycoumarin, was obtained by UV light irradiation.
Reprinted with permission from *J. Phys. Chem. B* **2021**, 125, 1674–1679. Copyright © 2021, American Chemical Society.

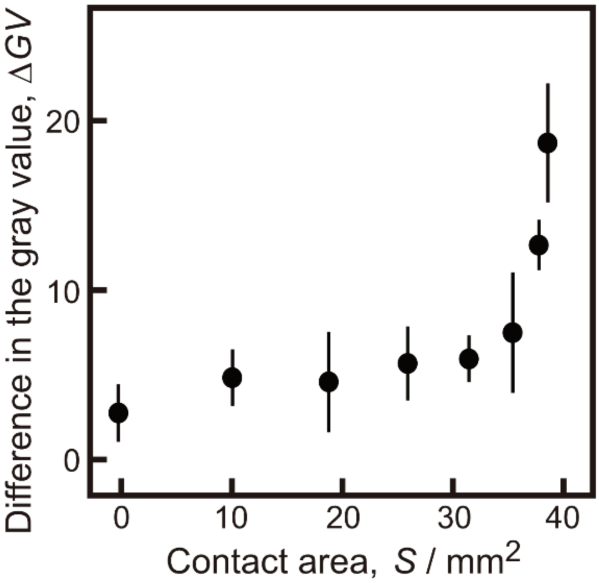

Figure 2-11. ΔGV of 7-hydroxycoumarin around the camphor object (Object I) at t_o = 40 s depending on S.
Reprinted with permission from *J. Phys. Chem. B* **2021**, 125, 1674–1679. Copyright © 2021, American Chemical Society.

The concentration of camphor (C_{es}) estimated by ΔGV corresponds to the distribution of camphor molecules on the SDS aqueous surface. As the disk is composed of 1 w/w% 7-hydroxycoumarin and 99 w/w% camphor, i.e., C_{es} = 99C_{hc} = 99 ×

$1.02\Delta GV$, C_{es} was estimated by ΔGV as **eq 2-3**.

$$C_{\mathrm{es}} = 100.98\ \Delta GV. \tag{2-3}$$

Figure 2-12 shows C_{es} of the aqueous solution near the camphor object (Object I) depending on S. As S increases, C_{es} was slightly increased at $S \leq 35.3$ mm^2, but drastically increased at $S \geq 37.7$ mm^2. According to Evaluation I, the threshold value of the camphor concentration between no motion and oscillatory motion was estimated to be ~ 0.5 mM at $S = 18.9$ mm^2.

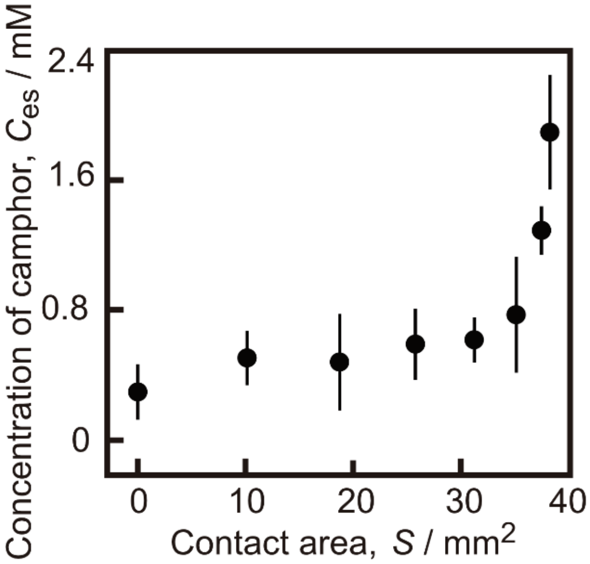

Figure 2-12. Estimated C_{es} near the camphor object (Object I) depending on S. Reprinted with permission from *J. Phys. Chem. B* **2021**, 125, 1674–1679. Copyright © 2021, American Chemical Society.

To confirm the threshold value of the camphor concentration between no motion and oscillatory motion by using the other method, Evaluation II was performed. To evaluate the concentration based on the absorbance of camphor, the relationship between the absorbance (A) and camphor concentration (C_{cp}) was measured by UV-Visible spectrophotometer at 283 nm which was the wavelength at the maximum absorbance for camphor aqueous solutions. A is linearly proportional to C_{cp}, as shown in **Figure 2-13**, and as a result, **eq 2-4** is obtained.

$$C_{cp} = 20.16\,A \qquad (2\text{-}4)$$

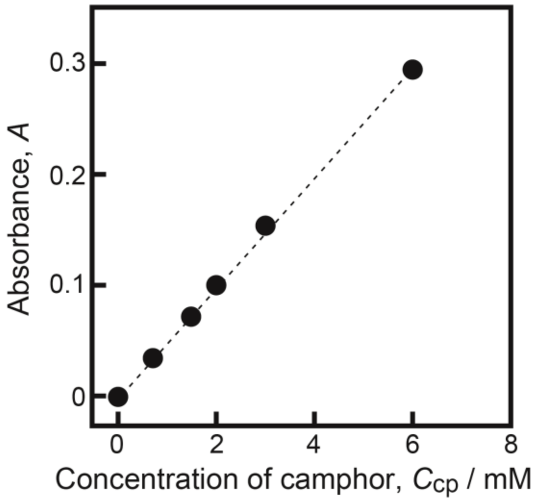

Figure 2-13. Calibration curve for the absorbance (A) *versus* the concentration of camphor (C_{cp}). The calibration curve was obtained from 10 mM SDS aqueous solution including camphor with different concentrations.
Reprinted with permission from *J. Phys. Chem. B* **2021**, 125, 1674–1679. Copyright © 2021, American Chemical Society.

The concentration of camphor dissolved into the SDS aqueous phase, C_{cp}, was estimated from the absorbance of camphor (A) dissolved into 10 mM SDS solution based on **eq 2-4**. **Figure 2-14** shows C_{cp} at $t_o = 40$ s as a function of S. C_{cp} was increased with an increase in S at $S > 18.9$ mm^2, but did not change very much at $S \leq 18.9$ mm^2, the threshold value of camphor concentration between no motion and oscillatory motion was estimated as 0.2 mM at $S = 18.9$ mm^2. The nature of the relationship between S and C_{cp} was similar to that of the S dependent C_{es}. Therefore, the threshold value of camphor concentration between no motion and oscillatory motion was regarded to be 0.2 ~ 0.5 mM according to Evaluation I and Evaluation II.

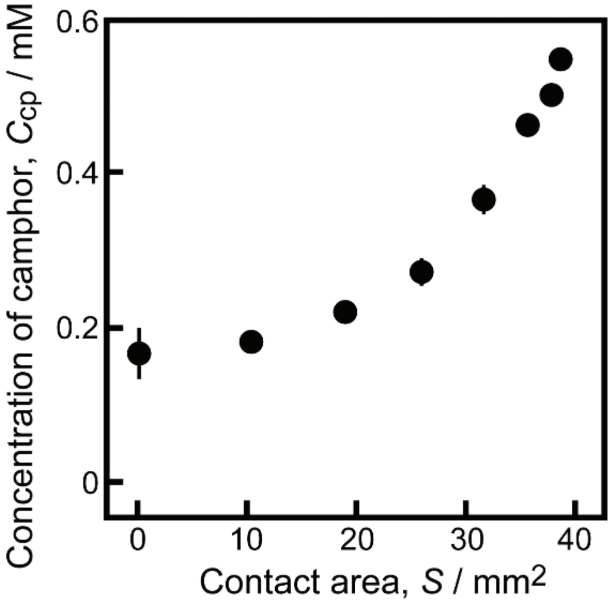

Figure 2-14. Concentration of camphor (C_{cp}) at t_o = 40 s after the addition of a camphor object (Object I) on the surface of the SDS aqueous solution depending on S. Reprinted with permission from *J. Phys. Chem. B* **2021**, 125, 1674–1679. Copyright © 2021, American Chemical Society.

The surface tension for 10 mM SDS aqueous solution after the addition of the different concentrations of camphor was measured to clarify the physicochemical significance of the maximum speed of oscillatory motion, as indicated in **Figure 2-15**. With an increase in the concentration of camphor, the surface tension was decreased. The difference in the surface tension between mixture of 10 mM SDS and 10 mM camphor aqueous solution and 10 mM SDS without camphor was ~ 2 mN m^{-1}.

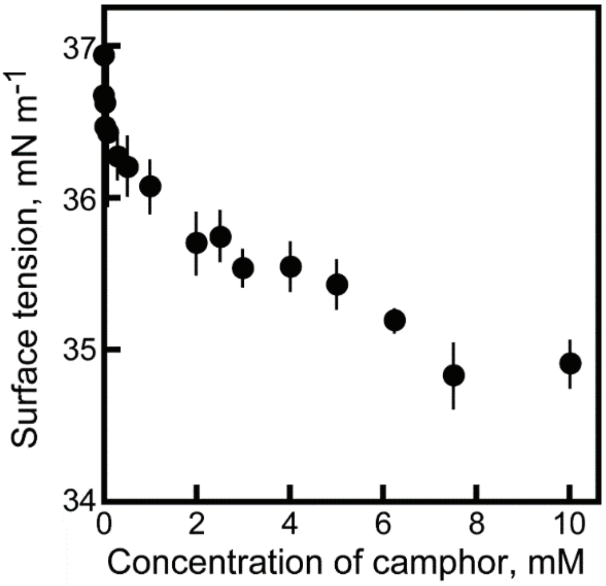

Figure 2-15. Surface tension of 10 mM SDS aqueous solution with different concentrations of camphor.
Reprinted with permission from *J. Phys. Chem. B* **2021**, 125, 1674–1679. Copyright © 2021, American Chemical Society.

2.4 Discussion

According to the experimental results and related papers [2, 11, 26-30], I discuss the mechanism underlying bifurcation between no motion and oscillatory motion of the camphor object I on the surface of 10 mM SDS aqueous phase based on the kinetics of camphor molecules around the camphor object. The driving force for self-motion of the camphor object on the surface of the SDS aqueous phase is difference in the surface tension around the camphor object. Camphor molecules and SDS molecules are important in the driving and suppressing forces of self-motion, respectively [28]. A small camphor disk (diameter: 3 mm) placed on the surface of 10 mM SDS aqueous phase displayed continuous motion in the previous study[31]. However, the camphor disk in this study displayed oscillatory motion. Such difference in the motion mode may be due to the different mass between both camphor disks.

Results in **Figures 2-3 ~ 2-5** suggest that the bifurcation between no motion and oscillatory motion depends on the amount of camphor molecules dissolved from the base of the camphor object (Object I). No motion was observed at $S < 18.9\ \mathrm{mm}^2$ suggests that a smaller amount of camphor molecules and a complex composed of camphor and SDS cannot diffuse to the surface of the SDS aqueous phase due to the SDS molecules adsorbed on water inhibits the development of the camphor molecules. Therefore, the camphor object cannot obtain the driving force. On the other hand, oscillatory motion was observed at $S \geq 18.9\ \mathrm{mm}^2$ suggests that a large amount of the complex composed of camphor molecules dissolved from object and SDS in the bulk phase can develop to the surface of the SDS aqueous phase. Therefore, the complex can regard as the source of the driving force for self-motion.

The constant frequency at $S \geq 25.9\ \mathrm{mm}^2$ in **Figure 2-5a** suggests that the complex molecules can develop to the surface of the SDS aqueous phase when the concentration of complex reaches a threshold value. In other words, the duration time for complex formation depends on the concentrations of camphor dissolved from the contact region of the basement in the camphor disk and SDS molecules in the bulk. The amount of camphor molecules has no effect on the duration time of complex formation. On the other hand, **Figure 2-6** suggests that the frequency is determined by the diffusion distance of the camphor molecules from the camphor disk.

Figures 2-5b and **2-6** suggest that maximum speed of the oscillatory motion is determined by the amount of complex composed of SDS and camphor molecules developed from the basement of the camphor object. In general, the amount of dissolution of a substance in a solvent is determined by the contact area between the substance and solvent. In addition, $v_{\max}$ of motion may be proportional to S, If the resistance is small enough to be ignored. **Figure 2-7** suggests that the driving force during the accelerated process of oscillatory motion at $S \geq 18.9\ \mathrm{mm}^2$ is independent of S since the profiles between the beginning and the end of the acceleration process are almost the same at different values of contact area. As shown in **Figures 2-11 and 2-14**, the threshold value of the ammonia concentration between no motion and oscillatory motion is regarded to be 0.2 ~ 0.5 mM. This range of value is similar to that reported in our previous research (0.8 mM) [34]. The frequency of oscillatory motion independent of S at $S \geq 25.9$ mm^2 may be seen in **Figure 2-5** since the camphor object starts to accelerate from the resting state when C_{es} reaches to a threshold value (0.2 ~ 0.5 mM) at the edge of the camphor object. On the other hand, the significant increase in C_{es} at $S \geq 37.7$ mm^2 suggests that the amount of the camphor molecules accumulated at the bottom of the camphor object is determined by contact area, S.

Figure 2-15 suggests that the driving force of oscillatory motion is the difference in the surface tension (~ 2 mN m^{-1}) between 10 mM SDS aqueous solution and SDS aqueous solution with addition of 10 mM camphor. The relationship between v_{max} (~10 mm s^{-1}) at S = 38.5 mm^2 and the difference in the surface tension (~ 2 mN m^{-1}) is reasonable because of the oscillatory motion of a camphor object on the surface of water phase of which the maximum speed (v_{max} ~ 100 mm s^{-1}) corresponding to the difference in the surface tension is ~ 17 mN m^{-1} [36]. Ten times of v_{max} can be induced by ten times of the difference in the surface tension as the driving force, since the speed depends on the driving force, $v = F/\mu$, where v is the speed, F is the driving force, μ is the friction coefficient when the speed reaches a constant value.

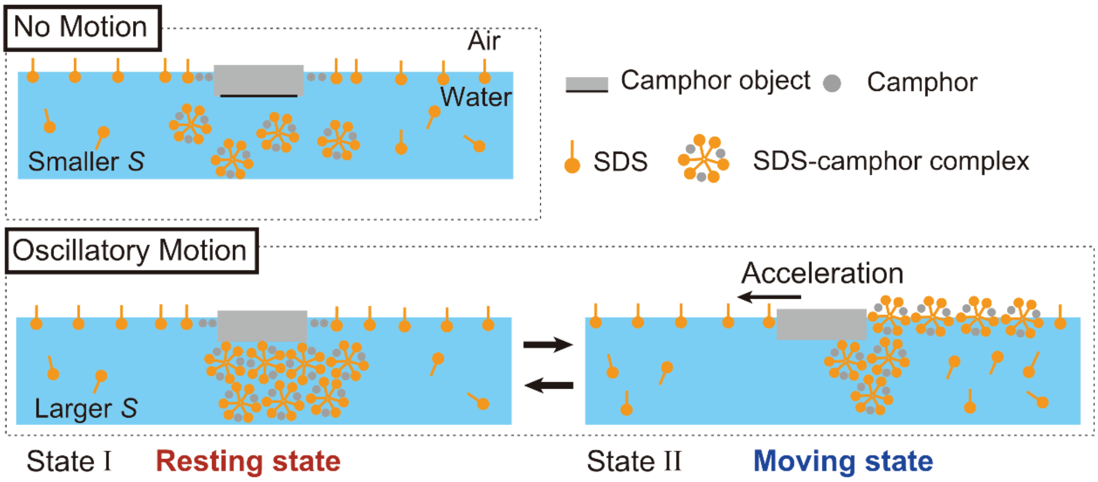

Figure 2-16. Schematic of the mechanisms of bifurcation between oscillatory motion and no motion for the camphor object (Object I).
Reprinted with permission from *J. Phys. Chem. B* **2021**, 125, 1674–1679. Copyright © 2021, American Chemical Society.

Figure 2-16 indicates a schematic diagram of the mechanism associated to the bifurcation between no motion and oscillatory motion for the camphor object I. In the case of a smaller *S* (**Figure 2-16a**), a large amount of SDS molecules in the aqueous phase react with the camphor dissolved from the edge of the disk to form the complexes, and then the complex composed of camphor and SDS molecules dissolved into the bulk phase. Because the surface tension of the saturated camphor aqueous solution (~ 55 mN m^{-1}) is significantly higher than that of 10 mM SDS aqueous solution (~ 37 mN m^{-1}), as a result, the SDS molecular layer adsorbed on the surface of the aqueous phase inhibits the development of the complexes and camphor molecules from the disk to the surface of the aqueous phase. Therefore, the camphor object cannot obtain the driving force induced by the difference in the surface tension. On the contrary, in the case of larger *S* (**Figure 2-16b**), the supply of the complex composed of SDS and camphor molecules around the object is higher than that of SDS molecules in the bulk phase. After the amount of complexes reaches a threshold value around the bottom of the disk (State I in **Figure 2-16b**), the complexes accumulated at the bottom of the object are spilled out form the bottom and then developed to the surface of the aqueous phase by excluding SDS molecules adsorbed in the bulk phase (State II in **Figure 2-16b**). As a result, the camphor object can be accelerated by the difference in the surface tension around the object. As the complexes accumulated at the bottom of the object remove from the bottom by the acceleration, the status of camphor object returns to State I from the acceleration state. Therefore, oscillatory motion was occurred since the alteration between State I and State II.

2.5 References

[1] M. Zarei, Self-Propelled micro/nanomotors for sensing and environmental remediation. *Small* **2018**, 14, 1800912.

[2] S. Nakata, V. Pimienta, I. Lagzi, H. Kitahata, N. J. Suematsu. Self-organized motion: Physicochemical design based on nonlinear dynamics. *RSC-ebook* **2018**.

[3] W. Flory, K. D. Krishna, S. Ayusman, Synthetic micro/nanomotors and pumps: Fabrication and applications. *Annu. Rev. Mater. Res.* **2016**, 46, 407−432.

[4] B. Jurado-Sanchez, J. Wang, Micromotors for environmental applications: A review. *Environ. Sci. Nano* **2018**, 5, 1530−1544.

[5] M. Guix, C. C. Mayorga-Martinez, A. Merkoci, Nano/micromotors in (Bio) chemical science applications. *Chem. Rev.* **2014**, 114, 6285–6322.

[6] M. N. Popescu, W. E. Uspal, C. Bechinger, P. Fischer, Chemotaxis of active Janus nanoparticles. *Nano Lett*. **2018**, 18, 5345–5349.

[7] Z. H. Huang, P. Y. Chen, G. L. Zhu, Y. Yang, Z. Y. Xu, L. T. Yan, Bacteria-activated Janus particles driven by chemotaxis. *ACS Nano* **2018**, 12, 6725–6733.

[8] D. Dattler, G. Fuks, J. Heiser, E. Moulin, A. Perrot, X. Yao, N. Giuseppone, Design of collective motions from synthetic molecular switches, rotors, and motors. *Chem. Rev.* **2020**, 120, 310−433.

[9] L. L. Ge, J. R. Cheng, X. H. Sun, J. L. Liu, D. Wei, R. Guo, Controlled group motion of anisotropic Janus droplets prepared by one-step vortex mixing. *ACS Appl. Mater. Interfaces* **2020**, 12, 14588−14598.

[10] E. Heisler, N.J. Suematsu, A. Awazu, H. Nishimori, Collective motion and phase transitions of symmetric camphor boats. *J. Phys. Soc. Japan* **2012**, 81, 74605.

[11] N. J. Suematsu, S. Nakata, Evolution of self-propelled objects: From the viewpoint of nonlinear science. *Chem. Eur. J.* **2018**, 24, 6308−6324.

[12] J. Adler, Chemotaxis in bacteria. *Science* **1966**, 153, 708.

[13] H. C. Berg, The rotary motor of bacterial flagella. *Annu. Rev. Biochem.* **2003**, 72, 19−54.

[14] C. V. Gabel, H. C. Berg, The speed of the flagellar rotary motor of escherichia coli

varies linearly with protonmotive force. *Proc. Natl. Acad. Sci. U. S. A.* **2003**, 100, 8748−8751.

[15] J. Wang, B. J. Toebes, A. S. Plachokova, Q. Liu, D. Deng, J. A. Jansen, F. Yang, D. A. Wilson, Self-propelled PLGA micromotor with chemotactic response to inflammation. *Adv. Healthc. Mater.* **2020**, 9, 1901710.

[16] O. E. Shklyaev, H. Shum, V. V. Yashin, A. C. Balazs, Convective self-sustained motion in mixtures of chemically active and passive particles. *Langmuir* **2017**, 33, 7873−7880.

[17] S. Kitawaki, K. Shioiri, T. Sakurai, H. Kitahata, Control of the self-motion of a ruthenium-catalyzed Belousov–Zhabotinsky droplet. *J. Phys. Chem. C* **2012**, 116, 26805−26809.

[18] D. Pantarotto, W. R. Browne, B. L. Feringa, Autonomous propulsion of carbon nanotubes powered by a multienzyme ensemble. *Chem. Comm.* **2008**, 1533−1535.

[19] Y. Watahiki, T. Nomoto, L. Chiari, T. Toyota, M. Fujinami, Experimental investigation of the self-propelled motion of a sodium oleate tablet and boat at an oil–water interface. *Langmuir* **2018***,* 34, 5487−5494.

[20] R. J. G. Löffler, M. M. Hanczyc, J. Gorecki, A hybrid camphor–camphene wax material for studies on self-propelled motion. *Phys. Chem. Chem. Phys.* **2019**, 21, 24852−24856.

[21] J. G. Gibbs, Y. P. Zhao, Design and characterization of rotational multicomponent catalytic nanomotors. *Small* **2009**, 5, 2304−2308.

[22] B. Nanzai, R. Ishikawa, M. Igawa, Spontaneous motion of *o*-toluidine droplets: repetitive motion of running and squashing. *Chem. Lett.* **2012**, 41, 609−611.

[23] S. Nakata, M. Nagayama, H. Kitahata, N. J. Suematsu, T. Hasegawa, Physicochemical design and analysis of self-propelled objects that are characteristically sensitive to environments. *Phys. Chem. Chem. Phys.* **2015**, 17, 10326−10338.

[24] L. Rayleigh, Measurements of the amount of oil necessary in order to check the motions of camphor upon water. *Proc. R. Soc. Lond*. **1997**, 47, 47364–47367.

[25] C. Tomlinson, On the motion of camphor on the surface of water. *Proc. R. Soc.*

London **1862**, 11, 575–577.

[26] S. Nakata, H. Yamamoto, Y. Koyano, O. Yamanaka, Y. Sumino, N. J. Suematsu, H. Kitahata, P. Skrobanska, J. Gorecki, Selection of the rotation direction for a camphor disk resulting from chiral asymmetry of a water chamber. *J. Phys. Chem. B* **2016**, 120, 9166−9172.

[27] Y. Karasawa, T. Nomoto, L. Chiari, T. Toyota, M. Fujinami, Motion modes of two self-propelled camphor boats on the surface of a surfactant-containing solution. *J. Colloid Interface Sci*. **2018**, 511, 184−192.

[28] J. Sharma, I. Tiwari, D. Das, P. Parmananda, V. Pimienta, Rotational synchronization of camphor ribbons in different geometries. *Phys. Rev. E* **2020**, 101, 052202.

[29] H. Morohashi, M. Imai, T. Toyota, Construction of a chemical motor-movable frame assembly based on camphor grains using water-floating 3D-printed models. *Chem. Phys. Lett.* **2019**, 721, 104−110.

[30] Y. Matsuda, N. J. Suematsu, H. Kitahata, Y. S. Ikura, S. Nakata, Acceleration or deceleration of self-motion by the Marangoni effect. *Chem. Phys. Lett.* **2016**, 654, 92−96.

[31] S. Nakata, M. Murakami, Self-motion of a camphor disk on an aqueous phase depending on the alkyl chain length of sulfate surfactants. *Langmuir* **2010**, 26, 2414−2417.

[32] A. Biswas, J. M. Cruz, P. Parmananda, D. Das, First passage of an active particle in the presence of passive crowders. *Soft Matter* **2020**, 16, 6138-6144.

[33] M. Frenkel, A. Vilk, I. Legchenkova, S. Shoval, E. Bormashenko, Mini-generator of electrical power exploiting the Marangoni flow inspired self-propulsion. *ACS Omega* **2019**, 4, 15265−15268.

[34] R. Tenno, Y. Gunjima, M. Yoshii, H. Kitahata, J. Gorecki, N. J. Suematsu, S. Nakata, Period of oscillatory motion of a camphor boat determined by the dissolution and diffusion of camphor molecules. *J. Phys. Chem. B* **2018**, 122, 2610−2615.

[35] Y. Xu, N. Takayama, E. Hua, S. Nakata, Oscillatory motion of a camphor object

on a surfactant solution. *J. Phys. Chem. B* **2021**, 125, 1674–1679.

[36] N. J. Suematsu, T. Sasaki, S. Nakata, H. Kitahata, Quantitative estimation of the parameters for self-motion driven by difference in surface tension. *Langmuir* **2014**, 30, 8101−8108.

Chapter 3. Self-propelled camphor disk dependent on the depth of the sodium dodecyl sulfate aqueous phase

3.1 Introduction

Many kinds of self-propelled objects for which the driving force is the difference in the surface tension around the object have been reported [1-17]. In these systems, Marangoni flow driven by the difference in the surface tension is observed around the objects [18-23], and convective flow occurs from the region with the lower surface tension to that with the higher surface tension at the air/aqueous interface [23-28]. The magnitude of Marangoni flow is determined by the depth of the water phase [29]. An opposite dependency on the depth of the water phase is displayed by a camphor boat as an asymmetric object and a camphor disk as a symmetric object, i.e., as the depth increases, the speeds of the camphor boat and the camphor disk was decreased and increased, respectively [30]. On the other hand, Marangoni flow can be suppressed by the surfactants dissolved in the water phase because of the reduced difference in the surface tension [31, 32]. However, it has been recently reported that the magnitude of Marangoni flow is recovered with a further increase in the concentration of surfactant over the critical micelle concentration (CMC) when a camphor disk is fixed on the aqueous surface [33, 34].

In this chapter, I examined the speed of self-motion for a camphor disk on the aqueous phase depending on the depth of the aqueous phase and the concentration of the surfactant (sodium dodecyl sulfate, SDS) in the aqueous phase. The results indicated that the speed of self-motion for the camphor disk on the shallower aqueous phase was lower than that on the deeper one at lower concentration of condition. However, the relationship between speed and depth was reversed in a higher concentration SDS aqueous solution below the CMC. The surface tension of the pure water and SDS aqueous phase at different depths and the diffusion of camphor molecules from the camphor disk were measured to evaluate the magnitude of the Marangoni flow. The results suggest that the speed of self-motion depended on the dissolution rate of camphor molecules from the camphor disk into the SDS aqueous phase forming the complex. In addition, the magnitude of Marangoni flow is affected by the friction from the bottom wall of the chamber.

3.2 Experimental section

Sodium dodecyl sulfate, SDS ($C_{12}H_{25}OSO_3Na$, purity > 98%, CAS 151-21-3), (+)–Camphor ($C_{10}H_{16}O$, > 98%, CAS 76-22-2), and 7-hydroxycoumarin ($C_9H_6O_3$, purity > 99%, CAS 93-35-6) were purchased from Sigma-Aldrich (St. Louis, MO), Wako Chemicals (Kyoto, Japan), and INDOFINE Chemical Company, Inc. (Stryker Lane, Hillsborough), respectively. Water used in this study was purified by filtering through active carbon, an ion-exchange resin, and a Millipore Milli-Q filtering system (Merck Direct-Q 3UV, Darmstadt, Germany; resistance: 18 MΩ cm). The different volume of SDS aqueous phases were poured into a glass Petri dish (diameter: 120 mm and depth: 23 mm) to setup the various values of the depth of the water. The effect of the depth of the aqueous phase, d (d = 2.8, 4.7, and 7.5 mm), on the speed of self-propelled camphor disk (diameter: 3 mm, thickness: 1 mm, and mass: ~ 5 mg) placed on the surface of SDS aqueous phase was examined at different concentrations of SDS. The concentrations of SDS aqueous solutions (C_{SDS}) in this study were 0, 0.1, 0.3, 0.5, 0.8, and 1 mM, which were lower than the critical micelle concentration of SDS (CMC ~ 8 mM). At least four examinations using new camphor disk were performed for each experimental condition to confirm the reproducibility of the experimental results. The movement of the camphor disk was recorded using a digital video camera (HDR-CX590, SONY, Tokyo, Japan; minimum time resolution, 1/30 s), and the movies were analyzed using a Java image processing and analysis program (ImageJ, National Institute of Health, Bethesda, MD, USA). The surface tension of aqueous solution was measured using a surface–interface tensiometer (CBVP-A3, Kyowa Interface Science Co. Ltd., Saitama, Japan). To indirectly visualize the distribution of camphor molecules in pure water or 1 mM SDS aqueous phase, I used the following three methods: (1) Plastic beads (DIAION, HP20S, average size: 200 μm, Mitsubishi Chemical Holdings Corp., Tokyo, Japan) homogeneously placed on the surface of the aqueous phase. (2) $CaCO_3$ powders (average size: 400 μm, Nihon Rikagaku Industry Co. Ltd., Kawasaki, Japan) homogeneously placed on the surface of the aqueous phase. (3) 1 w/w % 7-hydroxycoumarin (7-HC) was mixed with camphor in the disk as an indicator because it could be clearly observed by UV light irradiation (wavelength: 365 nm). Further, the density and solubility to water of the camphor were similar to those of 7-HC, and 7-HC disk on the water surface exhibited no motion [35]. All examinations were performed at 298 ± 2 K in an air-conditioned room.

3.3 Results

The time series of the speed of a self-propelled camphor disk floated on shallower (d = 2.8 mm) and deeper (d = 7.5 mm) aqueous phases with and without SDS is shown in **Figure 3-1**. The speed of camphor disk on the deeper aqueous phase was higher than that on the shallower phase at $C_{\mathrm{SDS}} = 0$. On the other hand, at $C_{\mathrm{SDS}} = 0.5$ mM, the speed of self-motion for the camphor disk was decreased by the addition of SDS, but the speed of camphor disk on the shallower aqueous phase was higher than that on the deeper one.

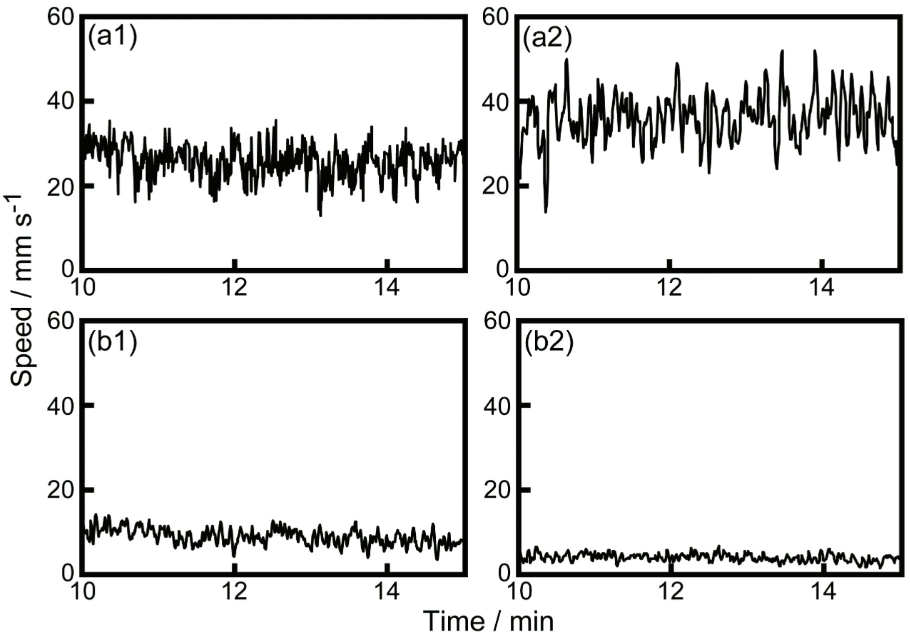

Figure 3-1. Time variation of the speed of a camphor disk on the aqueous phase (concentration of SDS: (a) 0 and (b) 0.5 mM) at d = (1) 2.8 and (2) 7.5 mm. Reprinted with permission from *Colloids Surf. A* **2022**, 635, 128087. Copyright © 2021 Elsevier B.V.

Figure 3-2 shows the average speed of self-propelled motion for the camphor disk depending on the concentration of SDS (C_{SDS}) at different values of d. The continuous motion of the camphor disk was observed under the experimental conditions of which the concentration of SDS was lower than the CMC. As indicated in **Figure 3-2**, the average speed of self-motion was decreased with an increase in C_{SDS}. The larger values of water depth lead to a higher speed at $C_{\mathrm{SDS}} \leq 0.1$ mM. On the contrary, the larger values of water depth lead to a smaller speed at $C_{\mathrm{SDS}} \geq 0.3$ mM. In other words, the relationship between speed and water depth was inverted around $C_{\mathrm{SDS}} = 0.2$ mM.

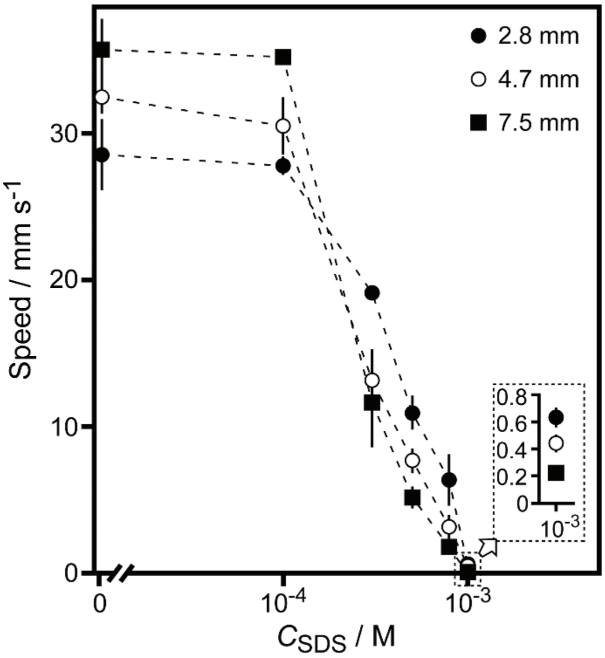

Figure 3-2. Average speed of the self-propelled motion of a camphor disk versus C_{SDS} depending on the concentration of SDS at different depths of the aqueous phase, *d* (filled circles: 2.8 mm, empty circles: 4.7 mm, and filled squares: 7.5 mm). Average values for the speed were obtained from 30 min observations, and the error bars were obtained from four examinations.
Reprinted with permission from *Colloids Surf. A* **2022**, 635, 128087. Copyright © 2021 Elsevier B.V.

To clarify the relationship between the average speed of self-motion and water depth, I measured the change in the surface tension of the aqueous phase after the addition of a camphor disk using a same glass Petri dish, as shown in **Figure 3-2**. **Figure 3-3a** shows the time series of the surface tension of the water after the addition of a camphor disk. The camphor disk placed on the surface of the water phase at $t = 0$. After that, the surface tension of the water was decreased with an increase in time at $t > 0$. A smaller value of *d* induces a larger decrease in surface tension. **Figure 3-3b** shows the time series of the surface tension for the 0.5 mM SDS aqueous phase. After the addition of the camphor disk, the surface tension also decreased with time. However, a larger *d* leaded to a larger decrease in surface tension.

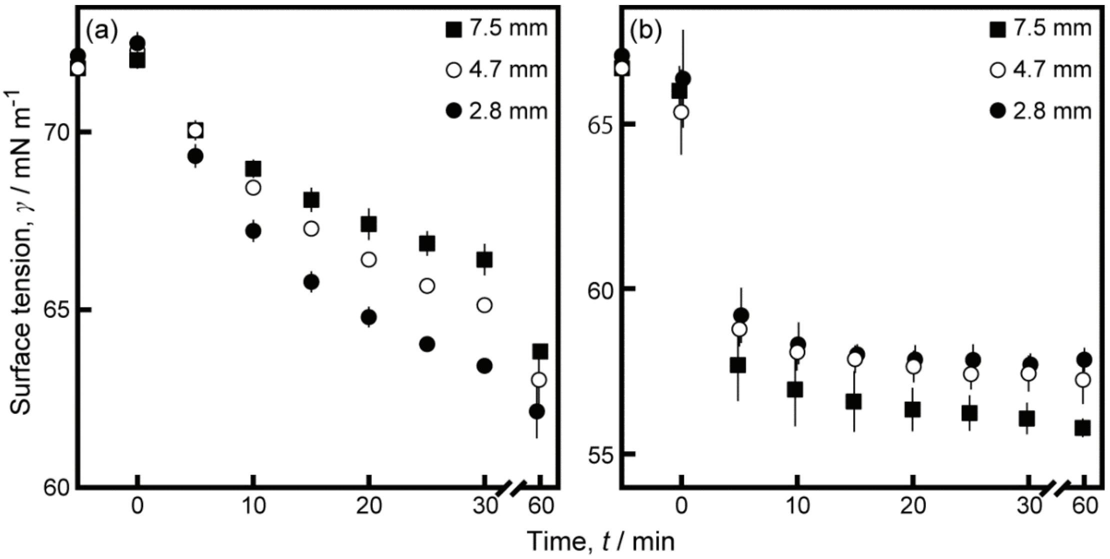

Figure 3-3. Time variation of the surface tension for (a) 0 and (b) 0.5 mM SDS aqueous phase at different values of *d* (filled circles: 2.8 mm, empty circles: 4.7 mm, filled squares: 7.5 mm). A camphor disk was placed on the aqueous phase at $t = 0$.

Reprinted with permission from *Colloids Surf. A* **2022**, 635, 128087. Copyright © 2021 Elsevier B.V.

To evaluate the effective diffusion coefficient (D) of camphor molecules developed from the disk, three kinds of visualization methods were performed. **Figure 3-4** shows the time variation of the snapshots for the camphor disk fixed on (a) pure water and (b) 1 mM SDS aqueous phase using method 1. The diffusion rate of camphor molecules on the surface of the pure water was significantly higher than that on the surface of 1 mM SDS aqueous phase.

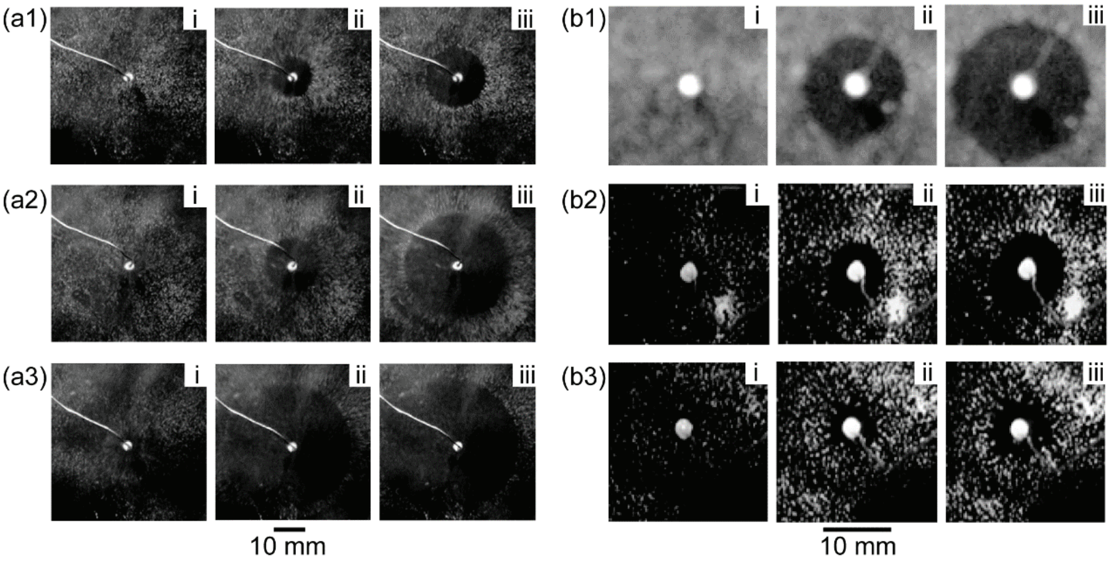

Figure 3-4. Time-series snapshots on the spatial distribution of visualization particles using method 1 when a camphor disk was fixed on (a) pure water and (b) 1 mM SDS aqueous solution at d = (1) 2.8, (2) 4.7, and (3) 7.5 mm (top view). The time intervals of each snapshot were (a) 1 and (b) 20 s.

Reprinted with permission from *Colloids Surf. A* **2022**, 635, 128087. Copyright © 2021 Elsevier B.V.

Based on the experimental results in **Figure 3-4**, I estimated effective diffusion coefficient (D). **Figure 3-5** shows the time series of diffusion distance, L, and L^2 at different values of d for (a) pure water and (b) 1 mM SDS aqueous solution. Here, L is the minimum value of the diffusion distance between the edge of the camphor disk and the diffusion edge of camphor molecules. The effective diffusion coefficient (D) was calculated based on the **eq 3-1**.

$$L^2 = 2Dt \tag{3-1}$$

That is, D was obtained from the slope of the graph of L^2 *vs.* t in **Figure 3-5**, as shown in **Table 3-1**. The value of D for camphor molecules on pure water was increased with an increase in d. However, the value of D for camphor molecules on the 1 mM SDS aqueous phase was decreased with an increase in d.

Table 3-1. Estimated values of D at d = 2.8, 4.7, and 7.5 mm based on the experimental results [37].

d / mm	D / mm^2 s^{-1} Water	 1 mM SDS
2.8	29.62	0.86
4.7	63.98	0.31
7.5	182.26	0.15

The methods 2 and 3 were used to check the validity of the result obtained by method 1. **Figure 3-6** shows the time variation of the snapshots of the camphor disk fixed on (a) pure water and (b) 1 mM SDS aqueous phase. Here, the methods 2 and 3 were adopted in (a) and (b), respectively. The method 2 could not be used for 1 mM SDS aqueous phase because the powders of $CaCO_3$ were not homogeneously distributed on the surface of the SDS aqueous phase. In addition, the method 3 could not be used for pure water because it is difficult to monitor the rapid diffusion of camphor molecules and 7-HC. The similar experimental results were obtained using the methods 2 and 3.**Figure 3-7** shows the time series of L and L^2 at different values of d for (a) pure water and (b) 1 mM SDS aqueous solution. The values of D obtained by method 1 were not significantly different from those obtained using methods 2 and 3, as shown in **Table 3-2**.

Table 3-2. Estimated values of D at d = 2.8, 4.7, and 7.5 mm based on the experimental results in **Figures 3-6 and 3-7** [37] .

d / mm	D / mm^2 s^{-1} Water	 1 mM SDS
2.8	36.93	1.46
4.7	156.14	0.63
7.5	293.04	0.07

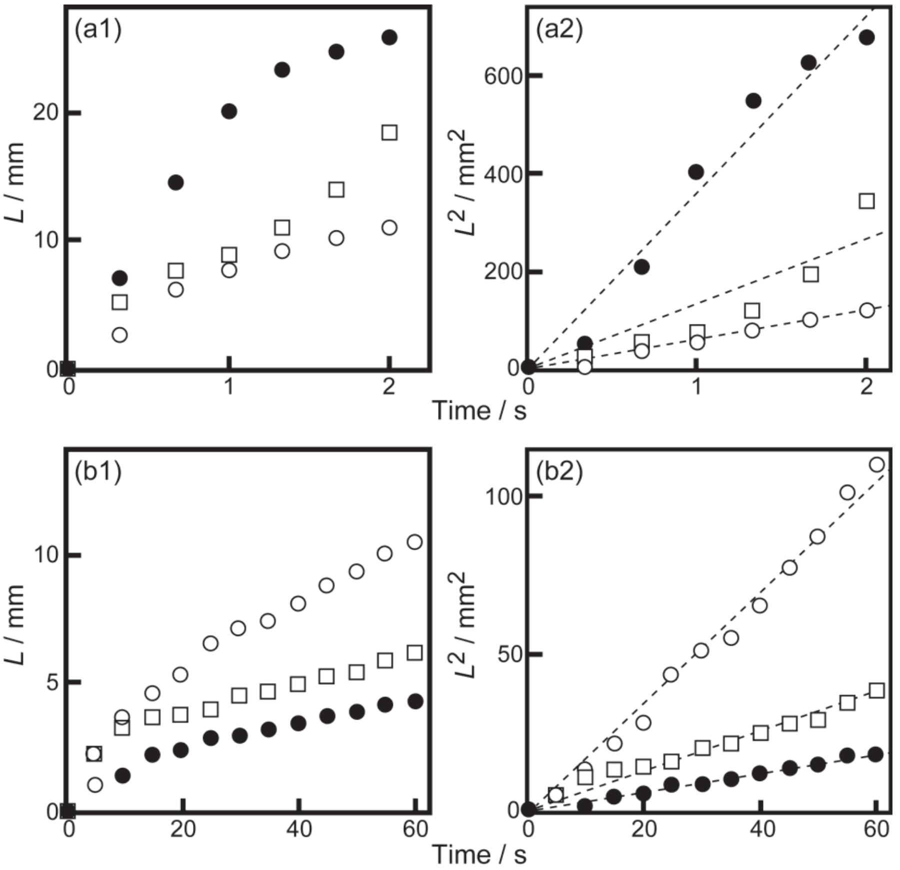

Figure 3-5. Time variation of (1) L and (2) L^2 at d = 2.8 (empty circle), 4.7 (empty square), and 7.5 mm (filled circle) for (a) pure water and (b) 1 mM SDS aqueous solution by using the method 1.

Reprinted with permission from *Colloids Surf. A* **2022**, 635, 128087. Copyright © 2021 Elsevier B.V.

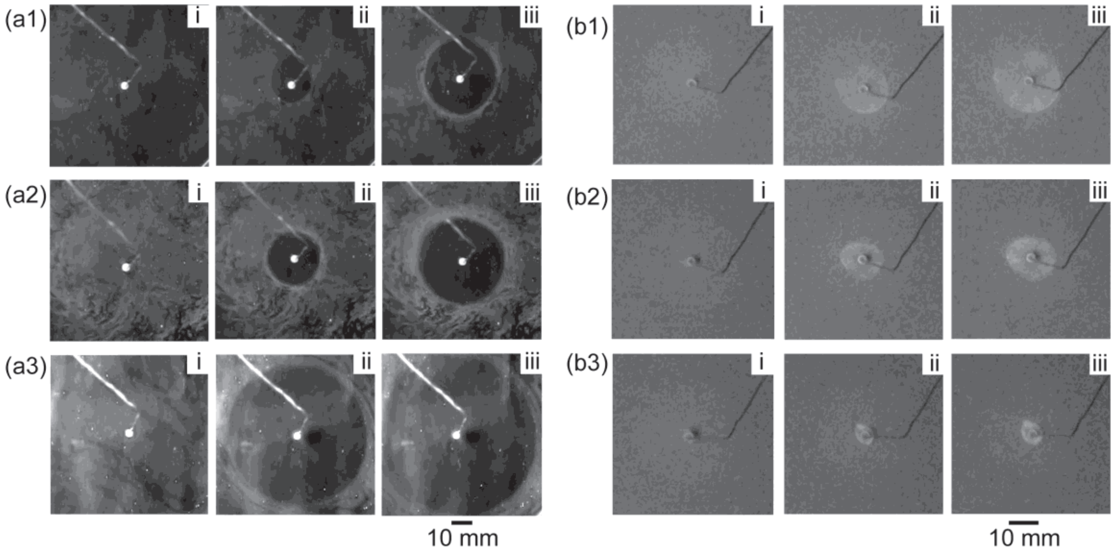

Figure 3-6. Time series of snapshots of visualization particles when a camphor disk was fixed on (a) pure water and (b) 1 mM SDS aqueous solution at d = (1) 2.8, (2) 4.7,

and (3) 7.5 mm (top view). The time intervals of each snapshot were (a) 1 and (b) 20 s. The methods 2 and 3 were used in (a) and (b), respectively.
Reprinted with permission from *Colloids Surf. A* **2022**, 635, 128087. Copyright © 2021 Elsevier B.V.

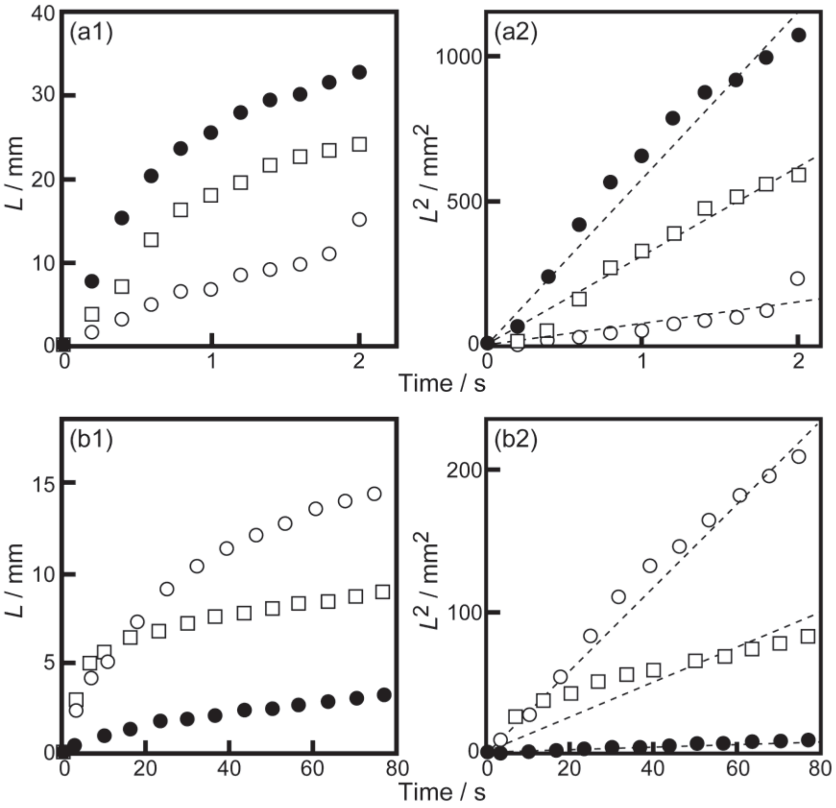

Figure 3-7. Time variation of (1) *L* and (2) L^2 at d = 2.8 (empty circle), 4.7 (empty square), and 7.5 mm (filled circle) for (a) pure water and (b) 1 mM SDS aqueous solution. The methods 2 and 3 were used in (a) and (b), respectively.
Reprinted with permission from *Colloids Surf. A* **2022**, 635, 128087. Copyright © 2021 Elsevier B.V.

3.4 Discussion

According to the experimental results and relative papers [23, 24, 30, 33-36], I discuss the mechanism of reversal relationship between depth and the average speed of self-motion for camphor disk at lower and higher concentrations of SDS. **Figure 3-3a** suggests that the difference in the surface tension, $\gamma = \gamma_s - \gamma_c$, around the camphor disk for the shallower pure water phase is lower than that for the deeper one. Here, γ_s is the surface tension of the aqueous phase, $\gamma_c \sim 55$ mN m^{-1} is the surface tension of the saturated camphor solution. In addition, **Figure 3-3b** suggests that the difference in the surface tension for the shallower SDS aqueous phase is larger than that for the deeper one. The higher speed of self-motion and the larger value of D are obtained on a larger difference in the surface tension since the larger value of γ can induce the stronger Marangoni flow.

Figure 3-4a indicates that the magnitude of Marangoni flow was increased with an increase in d of the pure water This result suggests that a larger magnitude of the flow leads to a higher speed of self-motion for camphor disk at $C_{\mathrm{SDS}} = 0$ [30]. In contrast, **Figure 3-4b** suggests that the decrease in the magnitude of Marangoni flow reduces the speed of self-motion for camphor disk with an increase in d on an 1 mM SDS aqueous phase.

To verify the discussion above, I designed a mathematical model for the time development of the camphor concentration induced by Marangoni convection and performed numerical calculation. For simplicity, a two-dimensional system $-x_0 \le x \le x_0$, $-h \le y \le 0$ was used into this model. Here the surface of the aqueous solution corresponds to the x-axis, and the vertical direction set as y-axis. h is the height of the system, which corresponds to the depth of the aqueous phase in experimental senction, and $2x_0$ is the horizontal length of the calculation area, which is set to be sufficiently large so that the side boundary should not affect the convection structure. Here, a camphor disk is fixed at the origin with radius r.

The dynamics of the flow field $\boldsymbol{v}(x, y) = v_x(x, y)\boldsymbol{e}_x + v_y(x, y)\boldsymbol{e}_y$, where $\boldsymbol{e}_x$ and $\boldsymbol{e}_y$ are the unit vectors in the x- and y-directions, respectively, are described by the Navier–Stokes equation:

$$\rho\left(\frac{\partial \boldsymbol{v}}{\partial t} + (\boldsymbol{v} \cdot \boldsymbol{\nabla})\boldsymbol{v}\right) = -\boldsymbol{\nabla} p + \eta \nabla^2 \boldsymbol{v}, \tag{3-2}$$

with the incompressible condition:

$$\boldsymbol{\nabla} \cdot \boldsymbol{v} = 0, \tag{3-3}$$

where ρ is the density of the aqueous solution, p is the pressure, and η is the viscosity of the aqueous solution.

The dynamics of the concentration fields, $c(x,y)$ for camphor and $s(x,y)$ for SDS, are described by the diffusion–reaction–advection equations as follows:

$$\frac{\partial c}{\partial t} + \boldsymbol{v} \cdot \boldsymbol{\nabla} c = D_0 \nabla^2 c - kcs^2 - ac\delta(y) + C_0 \Theta(|x| - R)\delta(y), \qquad (3\text{-}4)$$

$$\frac{\partial s}{\partial t} + \boldsymbol{v} \cdot \boldsymbol{\nabla} s = D_0 \nabla^2 s - kcs^2. \qquad (3\text{-}5)$$

In these equations, the second terms on the left-hand sides show the effect of convection. The first and second terms on the right-hand sides correspond to the diffusion and reaction between camphor and SDS, respectively. Notably, the diffusion described is not effective diffusion, but diffusion originating from thermal fluctuation. The third term on the right-hand side of Eq. (3-4) corresponds to the evaporation of camphor from the surface, and the fourth term represents the supply of camphor molecules from the camphor disk. Here, $\delta(y)$ is Dirac's delta function, and $\Theta(\cdot)$ is the Heaviside function. D_0, k, a, and C_0 are the diffusion coefficient, evaporation rate of camphor, reaction rate of camphor and SDS molecules, and supply rate of camphor molecules, respectively. The reaction term reflects the earlier report that one molecule of camphor forms a complex with two SDS molecules [34].

The Marangoni effect is introduced as a boundary condition for the flow field

$$\eta \left. \frac{\partial v_x}{\partial y} \right|_{y=0} = \left. \frac{\partial \gamma}{\partial x} \right|_{y=0} \qquad (3\text{-}6)$$

Here, γ is the surface tension, which is a function of the camphor and SDS concentrations.

$$\gamma = \gamma(c) = \gamma_0 - \gamma_1 c - \gamma_2 s, \qquad (3\text{-}7)$$

where γ_0, γ_1, and γ_2 are positive constants. This reflects that both the camphor and SDS molecules decrease the surface tension.

The nonslip boundary conditions are adopted for the flow field at the boundaries $y = -H$ and $x = \pm X_0$, and the Neumann boundary conditions are adopted for the concentration field. For the initial condition, I set $\boldsymbol{v} = \mathbf{0}$, $c = 0$, and $s = s_0$ over the entire region. Numerical calculations are performed using the stream function-vorticity method for the flow field and with the explicit method for the concentration fields. The discretization is performed with a time step of 10^{-3} and a spatial step of 0.2. The parameters are set as $D_0 = 1$, $a = 0.1$, $R = 1$, $C_0 = 1$, $\eta = 10$, $\gamma_1 = 1000$, $\gamma_2 = 100$, $k = 50$, and $X_0 = 250$. The parameter γ_0 need not be explicitly given in the calculation. The initial concentration of SDS, s_0, and the depth of the aqueous phase (H) are varied as parameters.

The representative results of the numerical simulation are indicated in **Figures 3-8 ~ 3-12**. **Figure 3-8** shows the camphor concentration fields $\boldsymbol{c}$ at the final stage for s_0 = (a) 0 and (b) 0.4 with H = (1) 20 and (2) 40. The camphor molecules are dissolved from the camphor disk fixed on the origin resulting in the higher concentration of camphor close to the origin. The concentration of camphor in the case with SDS in (b) is lower than that in the case without SDS in (a) because of the complex formed by SDS and camphor molecules in the aqueous phase. This can be confirmed from the SDS concentration field at the final stage obtained by the numerical simulation, as shown in **Figure 3-9**. The concentration of SDS in the phase close to the camphor disk is low because of the reaction between SDS and the camphor molecules diffused from the camphor disk. The concentration of camphor at $H = 20$ is higher than that at $H = 40$ since SDS molecules are consumed by reacting with camphor molecules, and the lack of SDS leads to an increase in the concentration of camphor at smaller H.

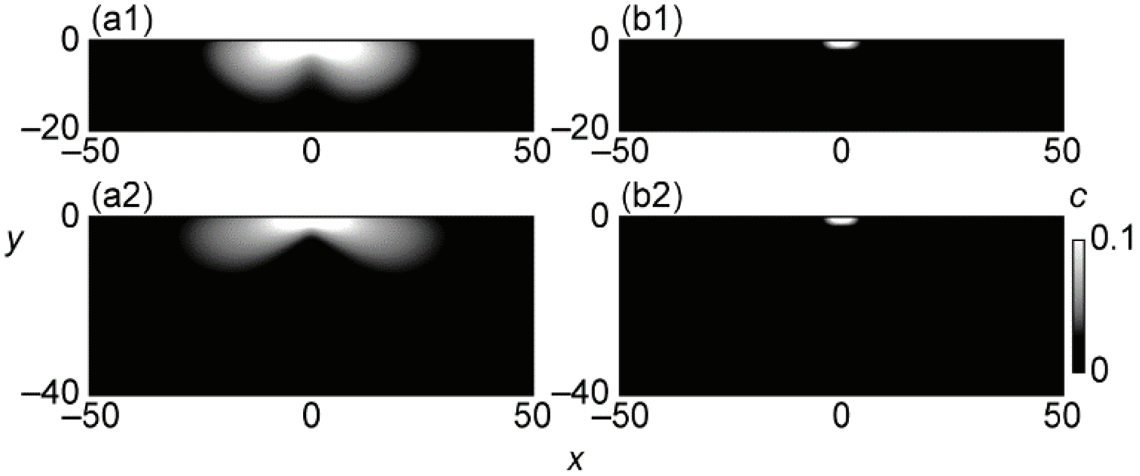

Figure 3-8. Snapshots of the camphor concentration field c in the region $-50 < x < 50$ and $-H < y < 0$ at $t = 100$. The initial concentration of SDS is s_0 = (a) 0 and (b) 0.4, and the depth of the aqueous phase is H = (1) 20 and (2) 40.
Reprinted with permission from *Colloids Surf. A* **2022**, 635, 128087. Copyright © 2021 Elsevier B.V.

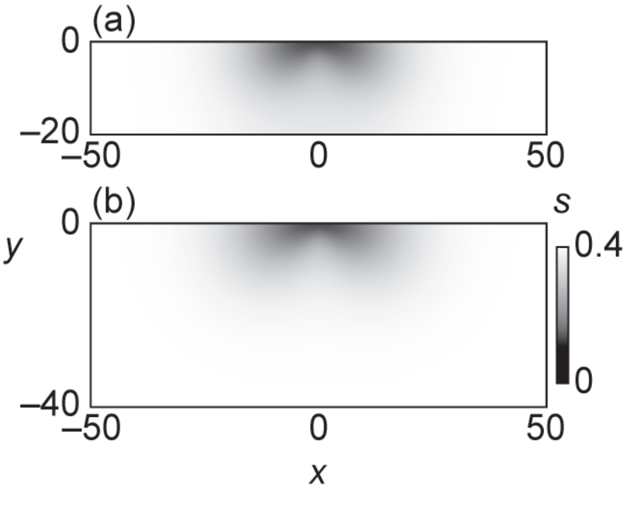

Figure 3-9. Snapshots of the SDS concentration field s in the region $-50 < x < 50$ and $-H < y < 0$ at $t = 100$. The initial concentration of SDS is $s_0 = 0.4$, and the depth of the aqueous phase is H = (a) 20 and (b) 40.
Reprinted with permission from *Colloids Surf. A* **2022**, 635, 128087. Copyright © 2021 Elsevier B.V.

In **Figure 3-10**, the flow fields $\boldsymbol{v}$ at the final stage are indicated for s_0 = (a) 0 and (b) 0.4 with H = (1) 20 and (2) 40. Since the camphor molecules reduce the surface tension of the aqueous phase, Marangoni flow occurs from the around camphor disk to the periphery close to the surface. In addition, the depth of the aqueous phase also affects the flow field. The amplitude and size of the convection rolls were increased with an increase in the depth *H*. In the case of pure water, Marangoni flow also occurs in the same direction. The magnitude of the flow for larger *H* is greater than that for smaller *H*, reflecting the concentration field of the camphor molecules.

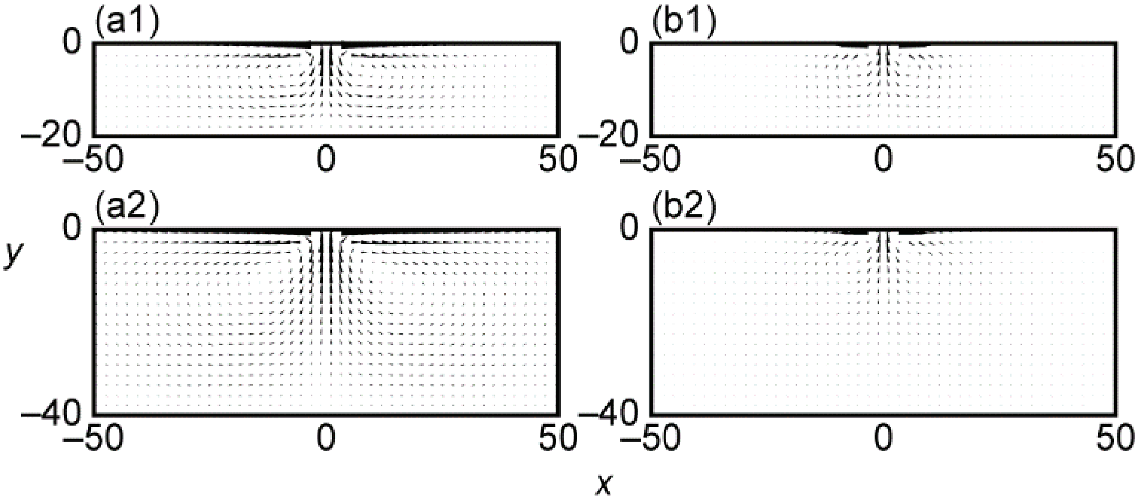

Figure 3-10. Snapshots of the flow field $\boldsymbol{v}$ in the region $-50 < x < 50$ and $-H < y < 0$ at $t = 100$. The initial concentration of SDS is s_0 = (a) 0 and (b) 0.4, and the depth of the aqueous phase is H = (1) 20 and (2) 40.
Reprinted with permission from *Colloids Surf. A* **2022**, 635, 128087. Copyright © 2021 Elsevier B.V.

To compare the results of the experiment with the numerical simulation, the front position $X(t)$ was defined as the position at the aqueous surface ($y = 0$), where $c = 10^{-6}$ is satisfied. **Figure 3-11** shows $X(t)$ for H = 10, 20, 30, and 40 is plotted for s_0 = (a) 0, (b) 0.2, (c) 0.4, and (d) 0.6. In the case of s_0 = (a) 0 and (b) 0.2, the front proceeds faster for the greater *H*. However, in the case of s_0 = (c) 0.4 and (d) 0.6, the front proceeds faster for the smaller *H*. In addition, I estimated the effective diffusion coefficient (*D*) based on the time variation of $\{X(t)\}^2$ with different *H* for each s_0 in **Figure 3-12**. **Table 3-3** shows the values for *D* for each *H* and s_0 obtained the data fitted with a linear function $\{X(t)\}^2 = 2Dt$ in the whole region of t. At $s_0 = 0$, the linear fitting worked well, while the plots of $\{X(t)\}^2$ were not linear to the time for finite s_0. The estimated values of D are under the experimental results qualitatively even if despite the diverge from the linear relation.

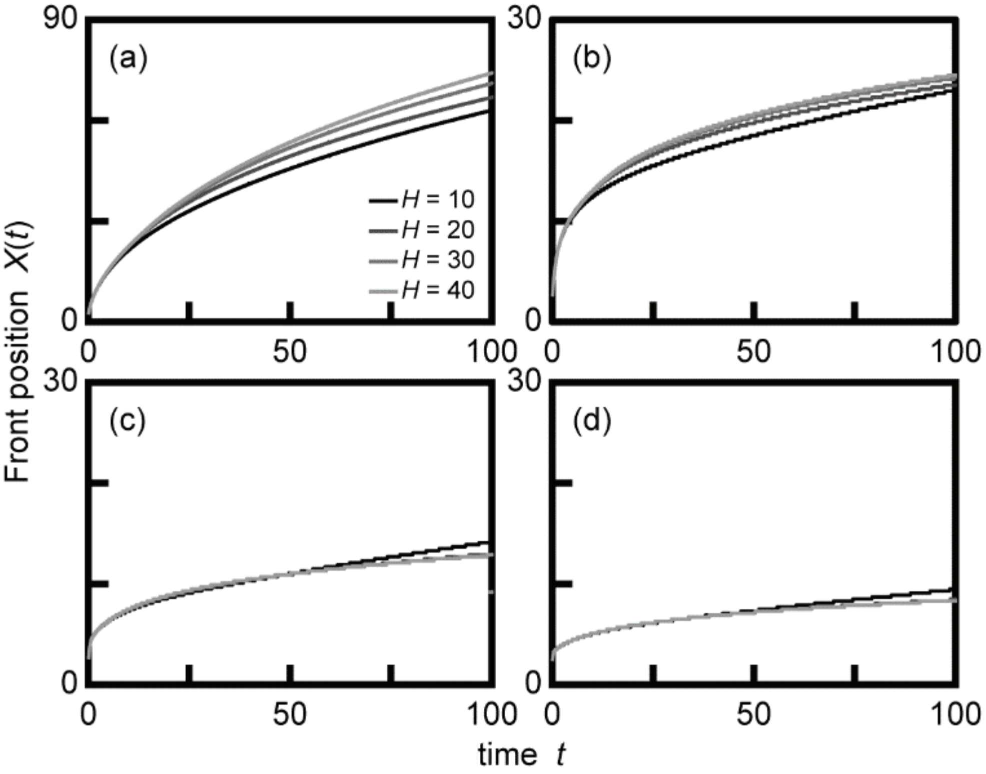

Figure 3-11. Time-series of the front position $X(t)$ for the initial concentration of SDS, s_0 = (a) 0, (b) 0.2, (c) 0.4, and (d) 0.6. The front position $X(t)$ for H = 10, 20, 30, and 40 is plotted with different grey values (dark to light for H = 10 to 40).
Reprinted with permission from *Colloids Surf. A* **2022**, 635, 128087. Copyright © 2021 Elsevier B.V.

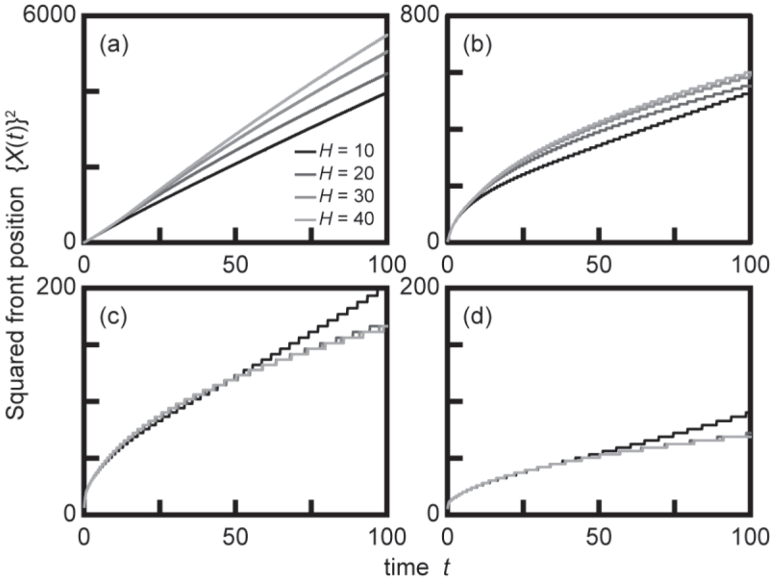

Figure 3-12. Time variation of the squared front position $\{X(t)\}^2$ for the initial concentration of SDS, s_0 = (a) 0, (b) 0.2, (c) 0.4, and (d) 0.6. $\{X(t)\}^2$ for H = 10, 20, 30, and 40 is plotted with different grey values (dark to light for H = 10 to 40).
Reprinted with permission from *Colloids Surf. A* **2022**, 635, 128087. Copyright © 2021 Elsevier B.V.

Table 3-3. Estimated values of D obtained by the fitting with a linear function from the data in **Figure 3-12** [37].

H	s_0			
	0	0.2	0.4	0.6
10	20.329	3.025	1.107	0.492
20	23.294	3.320	1.015	0.433
30	26.050	3.510	1.011	0.431

I consider that the dependence of $X(t)$ on H corresponds to the dependence of the effective diffusion coefficient, D, on the depth d observed in the experiments as shown in **Figure 3-4**. Based on the numerical calculations, the opposite dependency is explained as follows, at lower SDS concentration, a deeper aqueous phase induces a stronger Marangoni convection since the lower friction at the bottom wall. This stronger Marangoni convection induces a greater effective diffusion coefficient for the deeper aqueous phase. In contrast, at higher SDS concentrations, the amount of camphor molecules are lower in the deeper aqueous phase since the absence of SDS from complex formation with the camphor molecules. This induces strong Marangoni convection and a greater effective diffusion coefficient for the shallower aqueous phase. Combined, the opposite dependence of speed on the depth was determined by the competition between the consumption rate of SDS in the aqueous phase and the friction of the bottom wall.

3.5 References

[1] V. Pimienta, C. Antoine, Self-propulsion on liquid surfaces. *Curr. Opin. Colloid Interface Sci.* **2014**, 19, 290–299.

[2] C. H. Ooi, A. Van Nguyen, G. M. Evans, O. Gendelman, E. Bormashenkoe, N.-T. Nguyen, A floating self-propelling liquid marble containing aqueous ethanol solutions. *RSC Adv.* **2015**, 5, 101006–101012.

[3] R. Sharma, S. T. Chang, O. D. Velev, Gel-based self-propelling particles get programmed to dance. *Langmuir* **2012**, 28, 10128–10135.

[4] S. Nakata, V. Pimienta, I. Lagzi, H. Kitahata, N. J. Suematsu, Self-organized motion: Physicochemical design based on nonlinear dynamics. *The Royal Society of Chemistry,* Cambridge, **2019**.

[5] N. J. Suematsu, S. Nakata, Evolution of self-propelled objects: From the viewpoint of nonlinear science. *Chem. Eur. J.* **2018**, 24, 6308–6324.

[6] W. Fei, Y. Gu, K. J. M. Bishop, Active colloidal particles at fluid-fluid interfaces. *Curr. Opin. Colloid Interface Sci.* **2010**, 32, 57–68.

[7] R. J. G. Löffler, M. M. Hanczyc, J. Gorecki, A hybrid camphor-camphene wax material for studies on self-propelled motion. *Phys. Chem. Chem. Phys.* **2019**, 21, 24852–24856.

[8] K. Nagai, Y. Sumino, H. Kitahata, K. Yoshikawa, Mode selection in the spontaneous motion of an alcohol droplet. *Phys. Rev. E* **2005**, 71, 065301.

[9] H. Jin, A. Marmur, O. Ikkalaa, R. H. A. Ras, Vapour-driven Marangoni propulsion: continuous, prolonged and tunable motion. *Chem. Sci.* **2012**, 3, 2526–2529.

[10] M. Frenkel, G. Whyman, E. Shulzinger, A. Starostin, E. Bormashenko, Self-propelling rotator driven by soluto-capillary Marangoni flows. *Appl. Phys. Lett.* **2017**, 110, 131604.

[11] M. Frenkel, A. Vilk, I. Legchenkova, S. Shoval, E. Bormashenko, Mini-generator of electrical power exploiting the Marangoni flow inspired self-propulsion. *ACS Omega* **2019**, 4, 15265–15268.

[12] N. Bassik, B. T. Abebe, D. H. Gracias, Solvent driven motion of lithographically fabricated gels. *Langmuir* **2008**, 24, 12158–12163.

[13] T. Bansagi, Jr., M. M. Wrobel, S. K. Scott, A. F. Taylor, Motion and interaction of aspirin crystals at aqueous-air interfaces. *J. Phys. Chem. B* **2013**, 117, 43, 13572–13577.

[14] L. Wang, B. Yuan, J. Lu, S. Tan, F. Liu, L. Yu, Z. He, J. Liu, Self-propelled and long-time transport motion of PVC particles on a water surface. *Adv. Mater.* **2016**, 28, 4065–4070.

[15] A. Musin, R. Grynyov, M. Frenkel, E. Bormashenko, Self-propulsion of a metallic superoleophobic micro-boat. *J. Colloid Interface Sci.* **2016**, 479, 182–188.

[16] L. Qiao, D. Xiao, F. K. Lu, C. Luo, Control of the radial motion of a self-propelled microboat through a side rudder. *Sens. Actuator A Phys.* **2012**, 188, 359–366.

[17] F. Takabatake, N. Magome, M. Ichikawa, K. Yoshikawa, Spontaneous mode-selection in the self-propelled motion of a solid/liquid composite driven by interfacial instability. *J. Chem. Phys.* **2011**, 134, 114704.

[18] L. E. Scriven, C. V. Sternling, The Marangoni effect. *Nature*. **1960**, 187, 186−188.

[19] H. Kitahata, N. Yoshinaga, Effective diffusion coefficient including the Marangoni effect. *J. Chem. Phys*. **2018**, 148, 134906.

[20] T. Bickel, Spreading dynamics of reactive surfactants driven by Marangoni convection. *Soft Matter* **2019**, 15, 3644–3648.

[21] E. Lauga, A. M. J. Davis, Viscous Marangoni propulsion. *J. Fluid Mech.* **2012**, 705, 120–133.

[22] V. Vandadi, S. J. Kang, H. Masoud, Reverse Marangoni surfing. *J. Fluid Mech*. **2017**, 811, 612–621.

[23] H. Kitahata, S. Hiromatsu, Y. Doi, S. Nakata, M. R. Islam, Self-motion of a camphor disk coupled with convection. *Phys. Chem. Chem. Phys.* **2004**, 6, 2409−2414.

[24] H. Kitahata, H. Yamamoto, M. Hata, Y. S. Ikura, S. Nakata, Relaxation dynamics of the Marangoni convection roll structure induced by camphor concentration gradient. *Colloid Surf. A* **2017**, 520, 436−441.

[25] S. Sur, H. Masoud, J. P. Rothstein, Translational and rotational motion of disk-shaped Marangoni surfers. *Physics of Fluids* **2019**, 31, 102101.

[26] S. J. Kang, S. Sur, J. P. Rothstein, H. Masoud, Forward, reverse, and no motion of Marangoni surfers under confinement. *Phys. Rev. Fluids* **2020**, 5, 084004.

[27] M. M. Bandi, V. S. Akella, D. K. Singh, R. S. Singh, S. Mandre, Hydrodynamic signatures of stationary Marangoni-driven surfactant transport. *Phys. Rev. Lett*. **2017**, 119, 264501.

[28] M. Roché, Z. Li, I. M. Griffiths, S. Le Roux, I. Cantat, A. Saint-Jalmes, H. A. Stone, Marangoni flow of soluble amphiphiles. *Phys. Rev. Lett.* **2014**, 112, 208302.

[29] A. A. Nepomnyashchy, M. G. Velarde, P. Colinet, Interfacial phenomena and convection, *Chapman & Hall/CRC* Boca Raton, **2002**.

[30] Y. Matsuda, N. J. Suematsu, H. Kitahata, Y. S. Ikura, S. Nakata, Acceleration or deceleration of self-motion by the Marangoni effect. *Chem. Phys. Lett.* **2016**, 654, 92–96.

[31] J. B. Lewis, H. R. C. Pratt, Oscillating droplets. *Nature* **1953**, 171, 1155–1156.

[32] F. H. Garner, C. W. Nutt, M. F. Moutadi, Pulsation and mass transfer of pendent liquid droplets. *Nature* **1955**, 175, 603–605.

[33] Y. S. Ikura, R. Tenno, H. Kitahata, N. J. Suematsu, S. Nakata, Suppression and regeneration of camphor-driven Marangoni flow with the addition of sodium dodecyl sulfate. *J. Phys. Chem. B* **2012**, 116, 992–996.

[34] S. Nakata, R. Tenno, A. Deguchi, H. Yamamoto, Y. Hiraga, S. Izumi, Marangoni flow around a camphor disk regenerated by the interaction between camphor and sodium dodecyl sulfate molecules. *Colloids Surf. A* **2015**, 466, 40–44.

[35] Y. Xu, N. Takayama, E. Hua, S. Nakata, Oscillatory motion of a camphor object on a surfactant solution. *J. Phys. Chem. B* **2021**, 125, 1674–1679.

[36] S. Nakata and M. Murakami, Self-motion of a camphor disk on an aqueous phase depending on the alkyl chain length of sulfate surfactants. *Langmuir* **2010**, 26, 2414–2417.

[36] Y. Xu, N. Takayama, Y. Komasu, N. Takahara, H. Kitahata, M. Iima, S. Nakata. Self-propelled camphor disk dependent on the depth of the sodium dodecyl sulfate aqueous phase, *Colloids Surf. A* **2022**, 635, 128087.

Chapter 4. pH-sensitive oscillatory motion of a urease motor on the urea aqueous phase

4.1 Introduction

Various types of the self-propelled objects have been widely studied, not only to understand the mechanism of autonomous motion in living systems [1], but also to create the artificial motors that respond to the change in the external environments [2,3]. However, most self-propelled objects generally display unidirectional or random motion [2,3]. In contrast, nonlinear phenomena (i.e., oscillation, bifurcation, and synchronization) are frequently observed in living systems [4-8]. This suggests that the autonomy of self-propelled motors in living system is generally higher than that in living system, because nonlinear phenomena are often observed in living system [9]. In order to promote the autonomy and diversity of self-propelled object in non-living system, coupling of chemical reactions to self-propelled objects is one of the breakthrough ideas [9-12].

The characteristic behavior of nonlinearity can be created by introducing an enzyme reaction into the self-propelled systems, since the enzyme reaction generally displays highly nonlinear characteristics [13-15]. In the system of the urease-urea reaction, urea produces the alkaline products, that is, $(NH_2)_2CO + 3H_2O \xrightarrow{urease} HCO_3^- + 2NH_4^+ + OH^-$ [16-18]. A bell-shaped reaction rate as a function of pH is a well-known nonlinear property of enzyme involved systems [19]. The urease-catalyzed reaction of urea exhibits an autocatalytic process since the ammonia product enhances the pH of the urea aqueous solution under a non-buffered condition [20-22]. In this study, I introduce the urease-catalyzed reaction of urea into a self-propelled object, hereafter named a “urease motor” (see **Figure 4-1**), to induce oscillatory motion and bifurcation of the motion mode. The features of the self-motion (e.g., frequency and the maximum speed of oscillatory motion) for the urease motor are determined by the initial pH of the urea aqueous phase. The driving force of self-motion is the difference in the surface tension around the urease motor induced by the ammonia produced from the enzyme reaction. The mechanisms of oscillatory motion and synchronized oscillation of pH and speed of oscillatory motion was explained based on the driving force of self-motion and the enzyme activity of urease depending on pH.

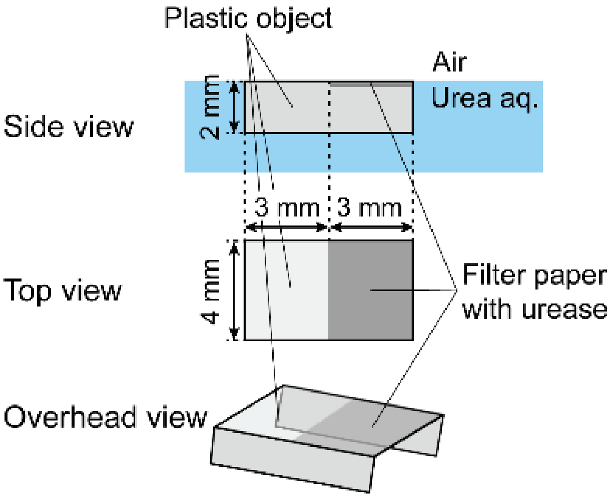

Figure 4-1. Schematic illustration of the urease motor used in this study.
Reprinted with permission from *Chem. Asian J.* **2021**, 16, 1762–1766. Copyright © 2021 Wiley-VCH GmbH.

4.2 Experimental section

4.2.1 Materials and methods

Urease from jack beans (purity > 98%; EC 3.5.1.5; CAS 9002-13-5; MW: 480 kDa; optimum pH: 7.4; minimum units: 45 U mg^{-1}) was supplied from Alfa Aesar (Lancashire, United Kingdom). Ammonium sulfate ($(NH_4)_2SO_4$; purity > 98%; CAS 7783-20-2) and Nessler's reagent were supplied from Sigma-Aldrich (St. Louis, MO, USA). Nessler's reagent is a mixed aqueous solution containing potassium iodide, potassium hydroxide, and mercuric chloride, which was used to check the presentation of ammonia. Sodium hydroxide (NaOH; purity> 98%; CAS 1310-73-2), methanol

(CH_3OH; purity> 98%; CAS 67-56-1), and Methyl red ($C_{15}H_{15}N_3O_2$; purity> 98%; CAS 493-52-7) were supplied from Wako Pure Chemical Industries, Ltd. (Osaka, Japan). Urea ($CO(NH_2)_2$; purity> 98%; CAS 57-13-6), 10.5 mol L^{-1} of sulfuric acid solution (H_2SO_4; purity> 98%; CAS 7664-93-9), and 28% of ammonia aqueous solution ($NH_4 \cdot H_2O$, CAS 7664-41-7) were supplied from Nacalai Tesque, Inc. (Kyoto, Japan). A polyvinylidene fluoride (PVDF) membrane (thickness: 160–170 μm; pore size: 0.45 μm) was supplied from Merck (Cork, Ireland) as a filter paper to immobilize urease.

4.2.2 Immobilization of the urease

The following steps was used to performed the immobilization of urease on the filter paper, a circular filter paper (diameter: 45 mm) was soaked into100% methanol (volume: 20 mL) for 30 seconds. Then the filter paper was immersed in pure water (volume: 40 mL) for 2 minutes to remove the methanol on the filter paper. Finally, a urease aqueous solution (10 U mL^{-1}; volume: 20 mL) was filtered through a filter paper to immobilize urease on the filter paper. The enzyme activity of the immobilized urease was measured by Nessler's reagent to test the immobilization result of the urease on the filter paper. To evaluate the enzyme activity of urease on the filter paper, I measured the absorbance for aqueous solutions with different concentrations of ammonium sulfate (volume: 4 mL) after the addition of the Nessler's reagent (volume: 1 mL). The absorbance, *A*, was measured by UV spectrophotometer (Shimadzu Corporation UV-1650, Kyoto, Japan). To induce a calibration curve on *A versus* ammonia concentration, 395 nm was selected since the maximum value of *A* was obtained at 395 nm at the range of the measured wavelength.

To calculate the enzyme activity of the urease on a filter paper, various pH urea solutions (volume: 1 mL) were first kept 25°C in a water bath with constant temperature for 5 minutes, and the urea-urease reaction was begun by adding a square filter paper immobilized with urease (10×10 mm^2). Then the urea aqueous solutions were stirred for 10 min at constant temperature (25°C) before the reaction was discontinued by 1 M sulfuric acid (volume: 1 mL). The absorbance for the aqueous solution after the addition of 1 mL Nessler's reagent, and 7 mL water was measured at 395 nm by the UV spectrophotometer.

4.2.3 Manufacture of the urease motor

A plastic object (length: 6 mm; width: 4 mm; high: 2 mm) which made by a 3D plotter (MASS CO., LTD. Roland, MonoFab, SRM-20, Yokohama, Japan) was used to make a fundamental structure for the urease motor, a filter paper with urease (length: 3 mm; width: 4 mm) was glued on the plastic object to manufacture the urease motor. The urease motor was floated on the surface of the urea aqueous phase (volume: 60 mL; concentration: 1 M; water level: 6 mm) in a Petri dish (diameter: 120 mm) at room temperature (T = 298 ± 2 K). The diagram of the urease motor used in this study is indicated in **Figure 4-1**.

4.2.4 Observation of the movement for urease motor

The movement of the urease motor placed on the surface of the urea aqueous phase was monitored using a digital video camera from a top view, and the movies were analyzed by the a Java image processing and analysis program "ImageJ 1.41" (National Institute of Health, Bethesda, MD, USA) on a PC. A pH meter supplied from HORIBA (pH-11B, Kyoto, Japan) was used to measure the pH of the urea solution, and the Wilhelmy plate method of the surface tensiometer supplied from Kyowa Interface Science Co., Ltd. (CBVP-A3, Saitama, Japan) was used to measure the surface tension of the ammonia aqueous solution at different concentration of ammonia. An pH indicator named methyl red was selected to evaluate the pH value of the urea aqueous phase. Here, a negligible amount of the methyl red (concentration = 10 μM) was added into the urea aqueous solution. The various initial pH urea solutions with acidic (3.0 to

6.5) and neutral (7.0 and 7.5) were prepared by H_2SO_4 solution and NaOH solution, respectively. Gray value (*GV*) of the color for the methyl red aqueous solutions at different pH was measured by ImageJ software to draw the calibration curve on gray value *vs.* pH value. The color of the methyl red aqueous solution (volume: 60 mL; concentration: 10 μM; water depth: 6 mm) in a glass Petri dish (diameter: 120 mm) at different pH was recorded with a digital video camera from top view. The color of the aqueous phase was changed from red (pH = 4.0) to yellow (pH = 6.0) with an increase in the pH of the methyl red aqueous solution. Here, pH of the methyl red aqueous phase was adjusted by sulfuric acid and sodium hydroxide, and *GV* was analyzed using by "ImageJ 1.41".

4.3 Results

Figure 4-2 shows the calibration curve on the absorbance (*A*) *vs.* the ammonia concentration of the aqueous phase. *A* was approximately proportional to the concentration of ammonia, according to the experimental result in **Figure 4-2**, **eq. 4-1** was obtained as the calibration curve.

$$C\ (\mu\text{M}) = 0.651\ A \qquad (4\text{-}1)$$

The amount of ammonia produced by the enzyme reaction was obtained from **eq 4-1**. Here, the amount of urease that catalyzes 1 μmol ammonia per minute at the required pH (25°C) is defined as one unit activity of urease. The initial pH depending on the enzyme activity of the urease on the filter paper is shown in **Figure 4-3**. With an increase in pH_{ini}, the enzyme activity was increased at $3.0 \le \text{pH}_{\text{ini}} \le 5.5$, however, the activity was decreased at $5.5 < \text{pH}_{\text{ini}} \le 7.5$. This is, pH_{ini} at the highest activity was 5.5.

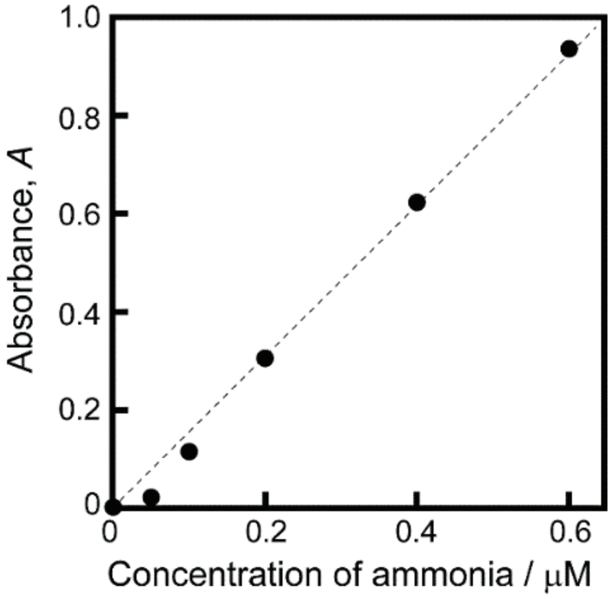

Figure 4-2. Calibration curve on the absorbance (*A*) of the ammonia solution *vs.* concentration of the ammonia.
Reprinted with permission from *Chem. Asian J.* **2021**, 16, 1762–1766. Copyright © 2021 Wiley-VCH GmbH.

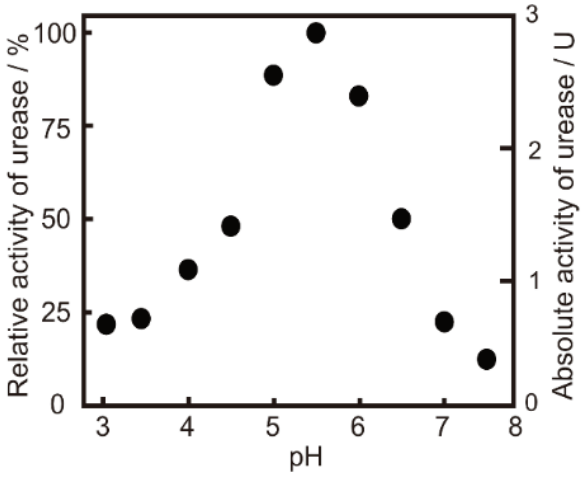

Figure 4-3. pH-dependent enzyme activity of the urease on a square filter paper (10 × 10 mm^2). The relative and absolute activities of urease are shown in the left and right vertical axes, respectively.
Reprinted with permission from *Chem. Asian J.* **2021**, 16, 1762–1766. Copyright © 2021 Wiley-VCH GmbH.

Then, I examined the speed of the self-motion for the urease motor on the urea aqueous phase at the different initial pH, pH_{ini}. **Figure 4-4** indicates the time series of the speed for the urease motor floated on urea aqueous solutions at various values of initial pH (pH_{ini} = 3.5, 5.0, 5.5, and 7.0). Here, the speed of the self-motion, $v = 0.5$ mm s^{-1} was defined as a threshold speed between no motion and motion to classify the mode of the motion. In other words, no motion denotes that the speed of the urease motor is less than 0.5 mm s^{-1}. Two kinds of motion mode, that is, no motion and oscillatory motion, were observed at different values of the initial pH. In this study, I defined that the oscillatory motion is the alternation process between the resting state and the moving state of the urease motor. No motion of the urease motor was observed at pH_{ini} = 3.5 and 7.0. In contrast, at pH_{ini} = 5.0 and 5.5, urease motor exhibits oscillatory motion. Maintain time of the oscillatory motion for the urease motor was at least 20 minutes.

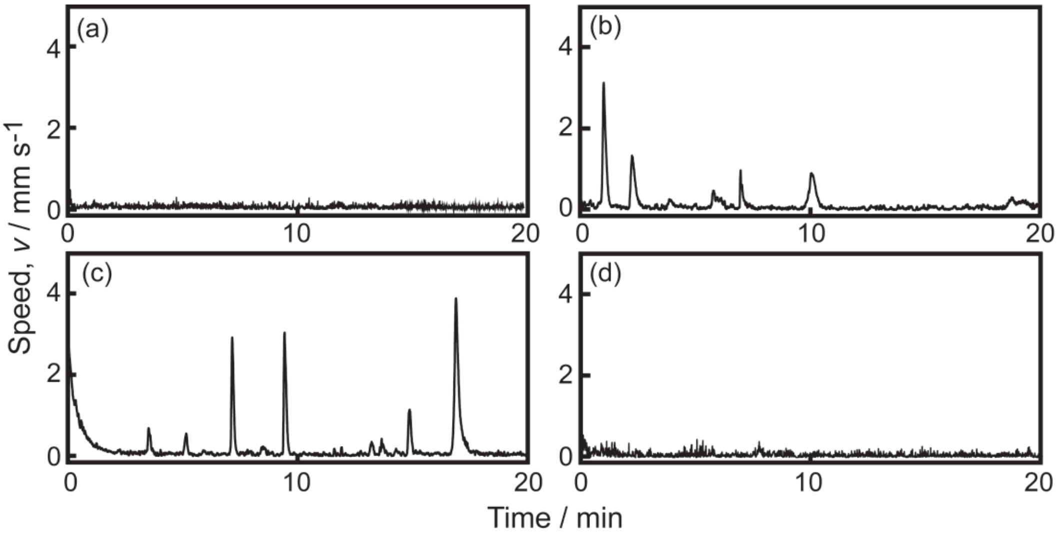

Figure 4-4. Time-series speed for the urease motor floated on the urea aqueous phase at different initial pH (a) 3.5, (b) 5.0, (c) 5.5, and (d) 7.0.
Reprinted with permission from *Chem. Asian J.* **2021**, 16, 1762–1766. Copyright © 2021 Wiley-VCH GmbH.

Figure 4-5 indicates features of the oscillatory motion ((a) average frequency (*f*), (b) average maximum speed (v_{max})) for the urease motor as a function of pH_{ini}. Here, the average frequency was calculated by the $f = 1/T$, T is the average period of the oscillatory motion. At $4.0 \leq \mathrm{pH_{ini}} \leq 6.5$, the urease motor exhibited the oscillatory motion. On the other hand, at $\mathrm{pH_{ini}} < 4.0$ and $\mathrm{pH_{ini}} > 6.5$, no motion was observed. In the other words, the bifurcation between the no motion and the oscillatory motion was occur around $\mathrm{pH_{ini}} = 4.0$ and $\mathrm{pH_{ini}} = 6.5$. In the range of oscillatory motion of the urease motor, as the initial pH increases, both of the frequency and maximum speed was increased at $4.0 \leq \mathrm{pH_{ini}} \leq 5.5$, but decreased at $5.5 \leq \mathrm{pH_{ini}} \leq 6.5$. In other words, maximum values of both f and v_{max} were observed at $\mathrm{pH_{ini}} = 5.5$. In addition, The relationship between f (and v_{max}) and the enzyme activity of urease on filter paper was also examined, as shown in **Figure 4-6**. As the enzyme activity increases, f and v_{max} were increased.

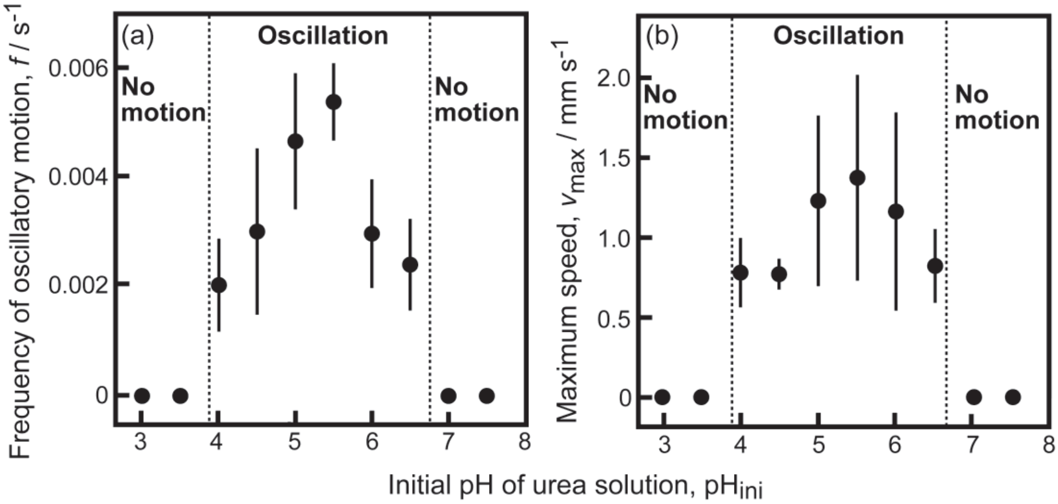

Figure 4-5. (a) Frequency and (b) maximum speed of the oscillatory motion as a function of the initial pH of the urea aqueous solution.
Reprinted with permission from *Chem. Asian J.* **2021**, 16, 1762–1766. Copyright © 2021 Wiley-VCH GmbH.

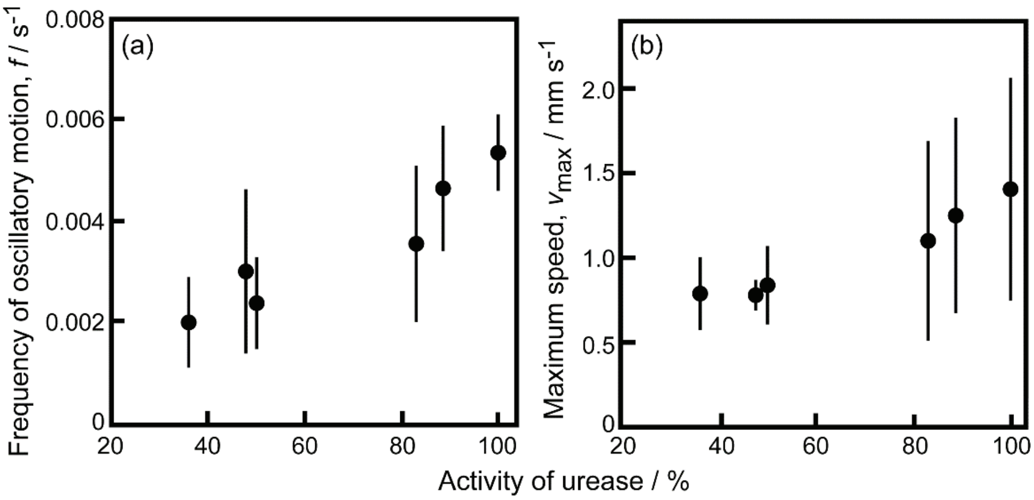

Figure 4-6. (a) Frequency and (b) the maximum speed of the oscillatory motion for the urease motor as a function of the enzyme activity of the urease.
Reprinted with permission from *Chem. Asian J.* **2021**, 16, 1762–1766. Copyright © 2021 Wiley-VCH GmbH.

To clarify the relationship between the state of the enzyme reaction and self-motion process of the urease motor, the pH of the urea aqueous solution near the tail of the urease motor and the speed of the urease motor were measured simultaneously. Here, a pH indicator named methyl red was adopted to calculate the local pH of the urea aqueous solution near the edge of the filter paper of the urease motor. The local value of the pH was calculated according to the calibration curve on pH of the urea aqueous solution *vs.* the gray value (*GV*), as indicated in **Figure 4-7**. Here, the gray value corresponding to the color of the urea aqueous solution at different pH was analyzed by the ImageJ software. Gray value is approximately proportional to pH, as shown in **eq 4-2**.

$$\mathrm{pH} = 0.16\ GV - 15.20 \qquad (4\text{-}2)$$

The time series of pH for the aqueous phase near the tail of the urease motor and the speed of the oscillatory motion at initial pH = 5.0 was shown in **Figure 4-8**. With the pH of the urea aqueous phase rapidly increased and reached a peak value of pH, the urease motor on the urea aqueous phase altered from the resting state to the moving state. When the speed of motion for the urease motor reached a peak value, pH of the urea aqueous solution rapidly decreased to the initial pH value, and speed of motion rapidly changed to zero. Therefore, the pH oscillation was synchronized with the speed of self-motion for the urease motor.

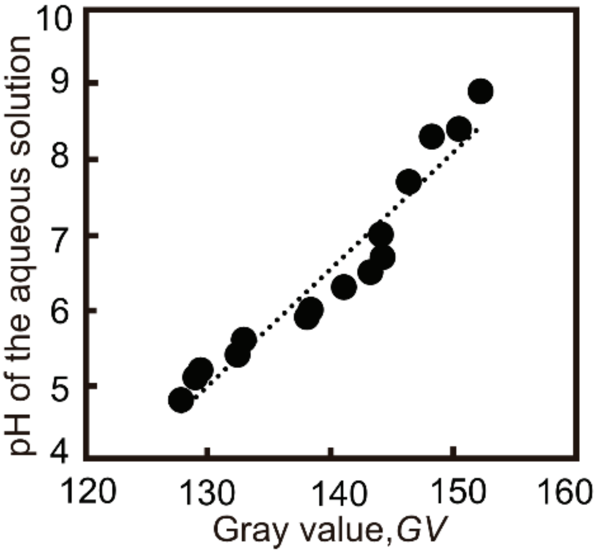

Figure 4-7. Calibration curve on the gray value *vs.* pH of the urea aqueous solution. Reprinted with permission from *Chem. Asian J.* **2021**, 16, 1762–1766. Copyright © 2021 Wiley-VCH GmbH.

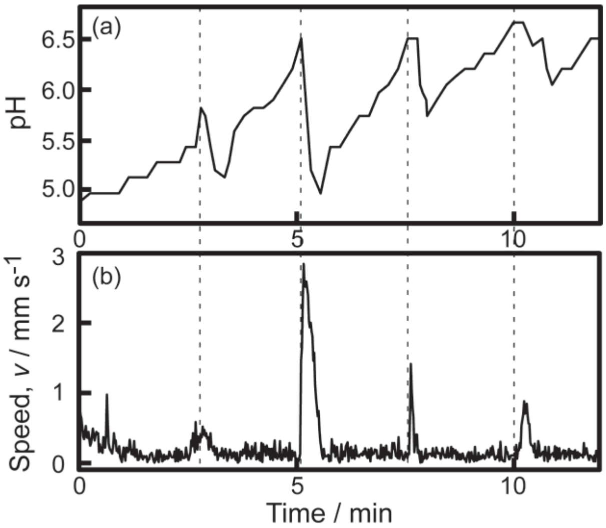

Figure 4-8. Time series of (a) pH of the aqueous phase near the tail of the urease motor and (b) speed of the urease motor. The measurement point of the gray value is ~2 mm

away from the edge of the filter paper with urease which is the opposite direction of the move.
Reprinted with permission from *Chem. Asian J.* **2021**, 16, 1762–1766. Copyright © 2021 Wiley-VCH GmbH.

To study the source of the driving force for the self-propelled motion, we measured the surface tension of the ammonia aqueous solution depending on the concentration of ammonia, as indicated in **Figure 4-9**. With an increase in the ammonia concentration, the surface tension of the aqueous solution was decreased. To test the effect of the additional chemicals on the surface tension of the water, I measured the surface tension of the water after the addition of the urea (concentration: 1 M), sulfuric acid (concentration: 50 μM), and methyl red (concentration: 10 μM). The additional chemicals (urea, sulfuric acid, and methyl red) have no influence on the surface tension of water, the results indicated in **Table 4-1**).

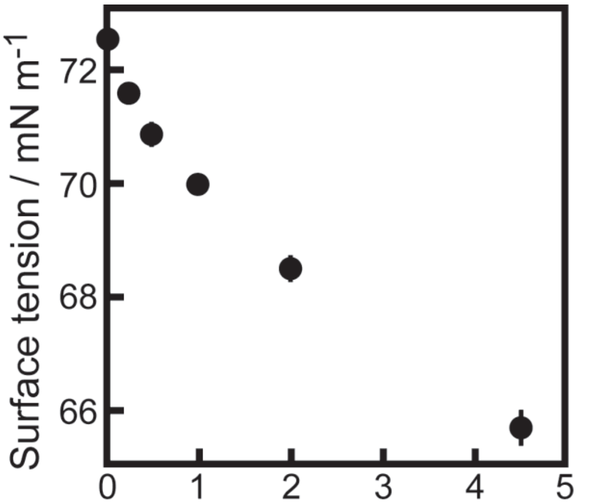

Figure 4-9. Surface tension of the ammonia aqueous solution depending on the concentration of ammonia.
Reprinted with permission from *Chem. Asian J.* **2021**, 16, 1762–1766. Copyright © 2021 Wiley-VCH GmbH.

Table 4-1. Surface tension of the aqueous solutions added additional chemicals [23].

Aqueous solutions	Surface tension / mN m^{-1}
Pure water	72.88
1 M urea solution	72.86
1 M urea + 10 μM methyl red + 50 μM sulfuric acid solution	73.09

I measured the maximum speed of a plastic object used in this study on the surface of the urea aqueous phase after the addition of a ammonia solution droplet with the different ammonia concentration to evaluate the threshold value of the ammonia concentration (C_{th}) between self-motion and no motion for the urease motor. A small-size droplet composed of the ammonia aqueous solution (volume: 10 μL) was dropped on the surface of the aqueous phase by a micropipette, the dropping position of the droplet is close to the edge of the resting plastic object. **Figure 4-10** shows the maximum speed of the plastic object on the surface of the urea aqueous phase as a function of the concentration of ammonia. The maximum speed of the plastic object was 4 mm s^{-1} after the addition of a pure water droplet. Here, I consider that the maximum speed (v_{max}) of 4 mm s^{-1} is attributed to the disturbance of the water surface because of the dropping of the pure water droplet. Therefore, I defined that the threshold speed (v_{th}) between self-motion and no motion of the plastic object was 4 mm s^{-1}. According to the threshold speed (v_{th}), I estimated that the threshold value of the ammonia concentration (C_{th}) was approximately 1 M, as indicated in **Figure 4-10**.

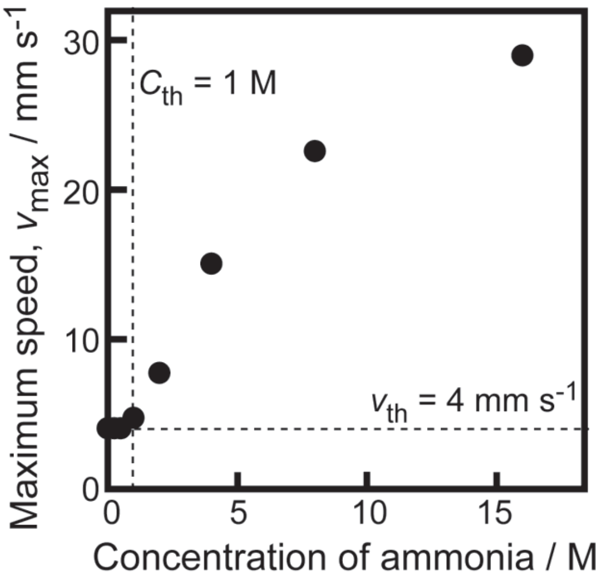

Figure 4-10. Maximum speed of the plastic object after addition of an ammonia droplet. The horizontal and vertical dashed lines denote the threshold value between motion and no motion, v_{th} = 4 mm s^{-1} and C_{th} = 1 M, respectively.
Reprinted with permission from *Chem. Asian J.* **2021**, 16, 1762–1766. Copyright © 2021 Wiley-VCH GmbH.

The time-series pH of the urea aqueous solution after the addition of a filter paper with urease was examined at various initial pH (pH_{ini} = 4.0, 5.5, 7.0), as indicated in **Figure 4-11**. pH was increased with an increase in time and converged to a constant value of pH = 9.0. Rapid change in pH of the urea aqueous solution was occurred at pH = 6.0.

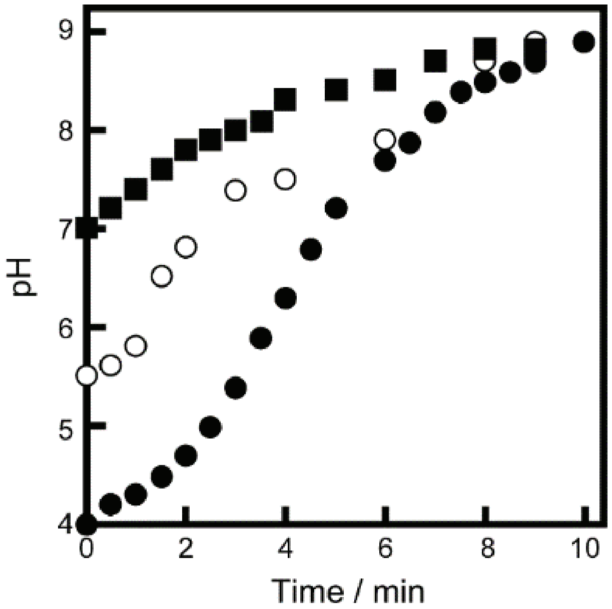

Figure 4-11. Time series of pH for the urea aqueous solution after the addition of filter paper with urease.
Reprinted with permission from *Chem. Asian J.* **2021**, 16, 1762–1766. Copyright © 2021 Wiley-VCH GmbH.

4.4 Discussion

According to the experimental results mentioned above and previous researches [11, 13, 19-22], the mechanism of the oscillatory motion and synchronization between pH oscillation and the speed of oscillatory motion was explained based on the origin of the driving force of self-motion and the bell-shaped curve activity of urease depending on pH.

Figures 4-5 and 4-6 suggest that the bifurcation between oscillatory motion and no motion depends on the enzyme activity of the urease, since the enzyme activity is sensitive to the pH of the urea aqueous phase. No motion at $pH_{ini} < 4.0$, and > 6.5 suggests that the reaction rates of the urea reaction at $pH_{ini} < 4.0$, and $pH_{ini} > 6.5$, are lower than those at $4.0 \leq pH \leq 6.5$, because of the low activity at lower and higher initial pH. It is difficult for the urease motor to produce ammonia as the source for the driving force of motion for the low activity of the urease. The largest value of the maximum speed and the frequency of the oscillatory motion at $pH_{ini} = 5.5$ are induced by the highest activity of urease. In other words, the highest production rate of ammonia occurred at $pH_{ini} = 5.5$.

The synchronized oscillation between the pH and the speed of the self-motion suggests that the sudden increase in pH leads to the acceleration of the resting urease motor and the decrease in the pH since the urease motor moves to a new position of the surface of the aqueous phase. Therefore, pH was reduced to a initial pH with the alteration from acceleration to no motion for the urease motor (see **Figures 4-7 and 4-8**).

Figure 4-9 suggests that the source of the driving force for the oscillatory motion is difference in the surface tension around the urease motor. Here, the difference in the surface tension was induced by the ammonia produced from the enzyme reaction of the urea. In addition, the bubble of carbon dioxide was not observed around the urease motor since the carbon dioxide is easily soluble into water phase and reversibly form a carbonic acid. Therefore, I focus only on the ammonia molecules as a source of the driving force for the self-propelled motion. **Figure 4-10** suggests that the threshold value of the ammonia concentration (C_{th}) between acceleration and no motion was 1 M.

From the previous results and discussion, the mechanism of the oscillatory motion depending on pH_{ini} was discussed based on the urease-urea enzyme reaction, as schematically indicated in **Figure 4-12**. The oscillatory motion is induced at $4.0 \leq pH_{ini} \leq 6.5$, where the urease motor alters to a resting state since the reaction rate of the enzyme reaction of the urea is low because of the lower pH_{ini}. The production of ammonia enhances the pH of the urea aqueous solution near the tail of the urease motor. the autocatalytic production of ammonia was induced by the increase in pH because of the increase in the enzyme activity (see **Figure 4-11**). Then, urease motor can be driven by the difference in the surface tension around the urease motor after the amount of the ammonia reaches the threshold concentration (C_{th}). Finally, the urease motor returns to the resting state from the moving state since the urease motor moves to a new position on the surface of the aqueous phase with initial pH. Therefore, oscillatory motion of the urease motor was observed since the repetition between resting state and moving state.

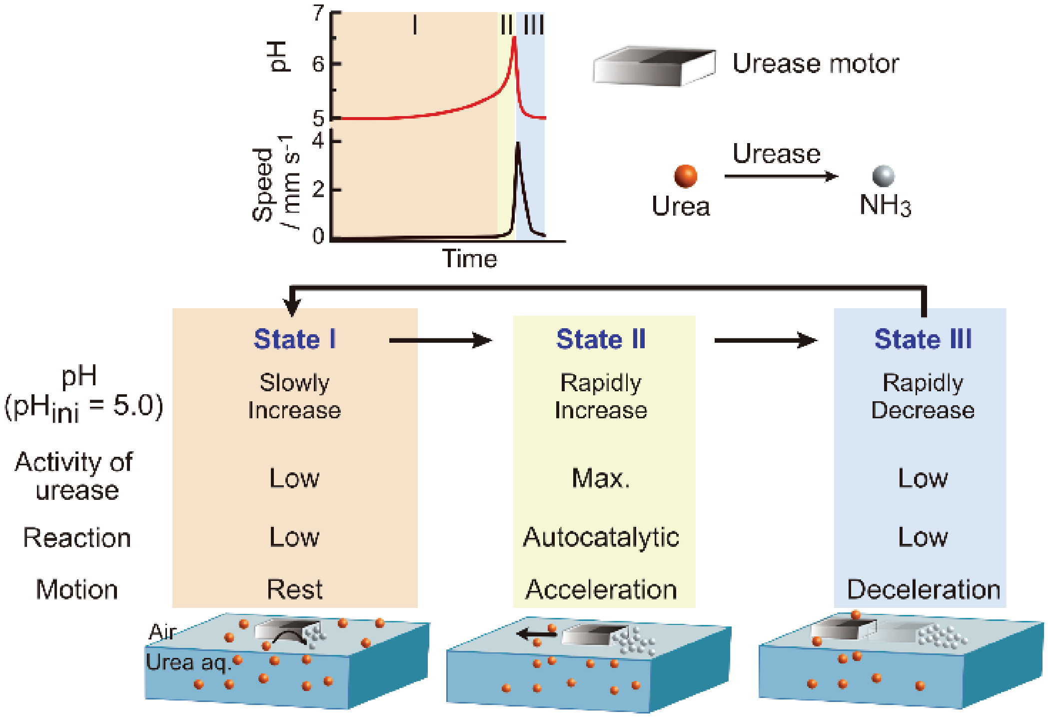

Figure 4-12. Schematic illustration of the mechanism of the pH oscillation and oscillatory motion.

Reprinted with permission from *Chem. Asian J.* **2021**, 16, 1762–1766. Copyright © 2021 Wiley-VCH GmbH.

4.5 References

[1] B. Haller, K. Jahnke, M. Weiss, K. Göpfrich, I. Platzman, J. P. Spatz, Autonomous directional motion of actin-containing cell-sized droplets. *Adv. Intell. Syst.* **2021**, 3, 2000190.

[2] F. Soto, E. Karshalev, F. Zhang, B. E. F. de Avila, A. Nourhani, J. Wang, Smart Materials for microrobots. *Chem. Rev.* **2021**, doi. Org /10.1021/ acs.chemrev. 0c00999.

[3] P. Illien, R. Golestanian, A. Sen, Fuelled motion: phoretic motility and collective behaviour of active colloids. *Chem. Soc. Rev.* **2017**, *46*, 5508−5518.

[4] I. R. Epstein, K. Showalter, Nonlinear chemical dynamics: oscillations, patterns, and chaos. *J. Phys. Chem.* **1996**, 100, 31, 13132−13147.

[5] Z. D. Li, Q. Yang, Systems and Synthetic Biology Approaches in Understanding Biological Oscillators. *Quant. Biol*. **2018**, 6, 1−14.

[6] K. Horikawa, K. Ishimatsu, E. Yoshimoto, S. Kondo, H. Takeda, Noise-resistant and synchronized oscillation of the segmentation clock. *Nature* **2006**, 441, 719−723.

[7] L. Glass, Synchronization and rhythmic processes in physiology. *Nature* **2001**, 410, 277−284.

[8] A. T. Winfree, The geometry of biological time. springer-verlag, New York, 2nd Ed., **2000**.

[9] S. Nakata, M. Nagayama, V. Pimienta, I. Lagzi, H. Kitahata, N. J. Suematsu, Theoretical and experimental design of self-propelled objects based on nonlinearity. *RSC*, **2018**.

[10] N. J. Suematsu, S. Nakata, Evolution of self-propelled objects: from the viewpoint of nonlinear science. *Chem. Eur. J.* **2018**, 24, 6308−6324.

[11] S. Nakata, Y. Irie, N. J. Suematsu, Self-propelled motion of a coumarin disk characteristically changed in couple with hydrolysis on an aqueous phase. *J. Phys. Chem. B* **2019**, 123, 4311−4317.

[12] S. Kitawaki, K. Shioiri, T. Sakurai, H. Kitahata, Control of the self-motion of a ruthenium-catalyzed Belousov–Zhabotinsky droplet. *J. Phys. Chem. C* **2012**, 116, 26805−26809.

[13] S. Nakata, M. Nomura, H. Yamamoto, S. Izumi, N. J. Suematsu, Y. Ikura, T. Amemiya, Periodic oscillatory motion of a self-propelled motor driven by decomposition of H_2O_2 by catalase. *Angew. Chem. Int. Ed.* **2017**, 56, 861−864.

[14] T. Amemiya, K. Shibata, M. Watanabe, S. Nakata, K. Nakamura, T. Yamaguchi, Phosphoglycerate mutase cooperates with chk1 kinase to regulate glycolysis. *Springer Nature*, **2020**, 23, 101206.

[15] T. V. Bronnikova, W. M. Schaffer, L. F. Olsen, Nonlinear Dynamics of the peroxidase−oxidase reaction. II. Compatibility of an extended model with previously reported model-data correspondences. *J. Phys. Chem. B* **2001**, 105, 310−321.

[16] L. B. Robert, Z. Burt, Jack bean urease: the first nickel enzyme. *J. Mol. Catal.* **1984**, 23, 263−294.

[17] E. Mack, D. S. Villars, The action of urease in the decomposition of urea. *J. Am. Chem. Soc.* **1923**, 45, 505−510.

[18] S. Sharma, J. B. Sumner, D. B. Hand, R. G. Holloway, Stimulation of flap endonuclease-1 by the bloom's syndrome protein. *J. Biol. Chem.* **1931**, 91, 333−341.

[19] I. N. Bubanja, T. Bánsági, A. F. Taylor, Kinetics of the urea–urease clock reaction with urease immobilized in hydrogel beads. *React. Kinet. Mech. Cat.* **2018**, 123, 177−185.

[20] G. Hu, J. A. Pojman, S. K. Scott, M. M. Wrobel, A. F. Taylor, Base-catalyzed feedback in the urea-urease reaction. *J. Phys. Chem. B* **2010**, 114, 14059−14063.

[21] E. Jee, T. Bánsági Jr, A. F. Taylor, J. A. Pojman, Temporal control of gelation and polymerization fronts driven by an autocatalytic enzyme reaction. *Angew. Chem. Int. Ed.* **2016**, 55, 2127−2131.

[22] D. Yang, J. H. Fan, F. Y. Cao, Z. J Deng, J. A. Pojman, L. Ji, Immobilization adjusted clock reaction in the urea–urease–H^+ reaction system. *RSC Adv.* **2019**, 9, 3514−3519.

[23] Y. Xu, L. Ji, S. Izumi, S. Nakata. pH-sensitive oscillatory motion of a urease motor on the urea aqueous solution. *Chem Asian J.* **2021**, 16, 1762–1766.

Chapter 5. General Conclusion

In this doctoral thesis, I constructed three self-propelled objects that show the characteristic nonlinear phenomena, which can respond to the internal and external environments.

In chapter 2, I designed a self-propelled object made of a camphor disk and a plastic sheet with different diameters. The camphor object on a sodium dodecyl sulfate (SDS) aqueous phase exhibits oscillatory motion and no motion at the different contact area of the basement of the object. The bifurcation between no motion and oscillatory motion depends on the kinetics of SDS and camphor molecules around the object. The features of motion were determined by the amount of camphor molecules and the formation of SDS–camphor complex. These results suggest that a novel self-propelled motor that displays characteristic motion can be created based on the kinetics of surfactant and camphor molecules.

In chapter 3, I studied the average speed of a self-propelled camphor disk floated on sodium dodecyl sulfate (SDS) aqueous phase at different depths. At the lower concentrations of SDS in the aqueous phase, the average speed of self-motion for the deeper aqueous phase was higher than that for the shallower aqueous phase. However, a reverse phenomenon of speed-dependent depth was observed at the higher SDS concentration. I consider that such a reverse phenomenon depends on the magnitude of Marangoni flow. In addition, the reverse phenomenon is qualitatively reproduced by numerical calculation based on the Navier-Stokes equation, the reaction-diffusion-advection equation, and the surface tension of camphor. Both the effective diffusion of camphor molecules and friction of the bottom wall also play an important role in the reverse phenomenon of the speed-dependent depth. These results suggest that a kind of self-propelled object that is sensitive to the basement shape of the aqueous phase can be created by changing the depth of the environment.

In chapter 4, I designed a simple self-propelled motor made of a plastic object and a filter paper with urease. The driving force for the oscillatory motion is the difference in the surface tension around the urease motor induced by the ammonia produced from the urease-catalyzed reaction of urea. The characteristics of self-propelled motion for the urease motor was determined by the initial pH of the urea aqueous phase, pH_{ini}. The largest values for the frequency and maximum speed depend on the bell-shaped activity-pH curve for urease. This study suggests that the oscillatory motion can be created by coupling the nonlinear enzyme reaction of the urea. In other words, the significant increase in the enzyme activity of urease at an optimum pH induces autocatalytic production of ammonia which is the source of the driving force for the self-propelled motion. In addition, the autocatalytic process in the enzyme reaction plays an important role in the generation of oscillatory motion from viewpoint of the nonequilibrium conditions. This study proposes a novel self-propelled motor based on a nonlinear reaction, that is, the autocatalytic process of the enzyme reaction.

In summary, I provided several strategies for designing self-propelled objects and explanations regarding the motion mechanism. It is significant to understand how self-propelled objects exhibit characteristic motion and to establish ways of controlling their motion. In the future, I am going to develop self-propelled objects that exhibit the characteristic motion by the molecular control and coupling of the chemical reaction. In addition, synchronization and collective motion in coupled with several numbers of symmetric or asymmetric self-propelled objects are going to study as future work to understand the mechanism of group motion of animals.

Acknowledgements

I would like to express my acknowledgement to all the people who had helped and supported me during my doctoral course.

First, I would like to pay my special appreciation to my supervisor, Professor Satoshi Nakata, for his patient guidance, enthusiastic encouragement and useful suggestions during my whole doctoral research life. He is such a nice, energetic and knowledgeable researcher who can always have a lot of innovative and unique ideas for the guidance of my study. His kindness and enthusiasm deeply affected me and helped me gradually adapt to the new study environment.

Secondly, I would like to especially thank Muneyuki Matsuo, Masakazu Kuze, Takero Matsufuji, and Nami Takayama, who taught me how to operate the experimental equipment safely. They always put forward many useful suggestions for my research and life, which helped me a lot.

Then, I am particularly grateful to Professors, Hua Er from North Minzu University, Lin Ji from Capital Normal University, Hiroyuki Kitahata from Chiba University, Shunsuke Izumi, and Makoto Iima from Hiroshima University, for their useful suggestion and discussion for my research.

Finally, my heartfelt gratitude goes to my dear family members and relatives. Especially, the big love and best support of my parents are an extremely great motivation for me to overcome the difficulties and complete my doctoral program.